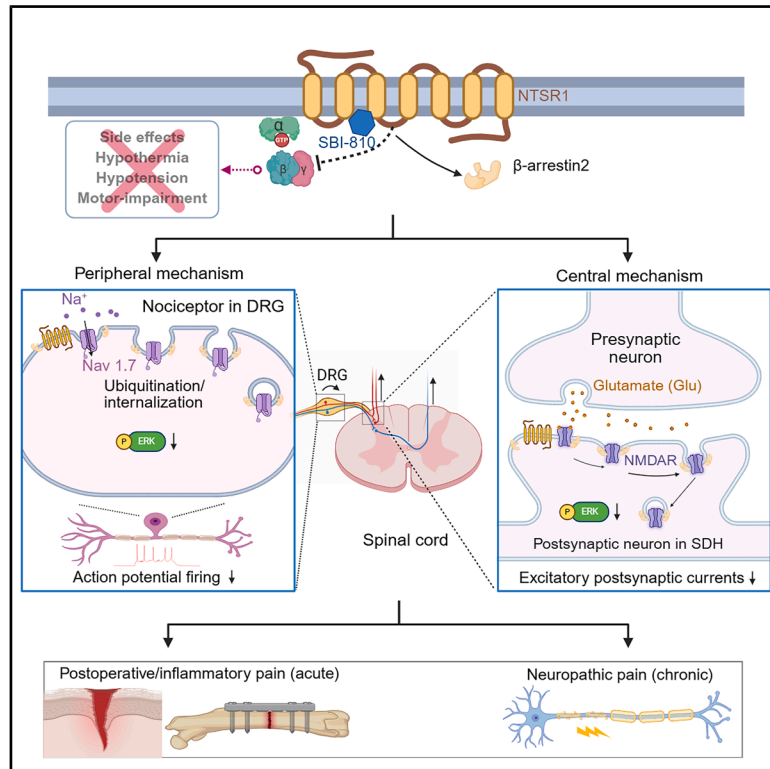


Arrestin-biased allosteric modulator of neurotensin receptor 1 alleviates acute and chronic pain

Graphical abstract



Authors

Ran Guo, Ouyang Chen, Yang Zhou, ..., William C. Wetsel, Lawrence S. Barak, Ru-Rong Ji

Correspondence

ru-rong.ji@duke.edu

In brief

SBI-810, an arrestin-biased allosteric modulator of neurotensin receptor 1, can effectively alleviate acute and chronic pain in rodent models via peripheral and central modulation and can also mitigate opioid withdrawal effects.

Highlights

- SBI-810 is a β -arrestin-2-biased allosteric modulator of neurotensin receptor 1
- Systemic or local SBI-810 injection inhibits acute and chronic pain in rodent models
- SBI-810 blocks peripheral and central sensitization in DRG and spinal cord neurons
- SBI-810 mitigates opioid abuse and does not impair motor and cognitive function

Article

Arrestin-biased allosteric modulator of neurotensin receptor 1 alleviates acute and chronic pain

Ran Guo,^{1,10} Ouyang Chen,^{1,2,10} Yang Zhou,² Sangsu Bang,¹ Sharat Chandra,¹ Yize Li,¹ Gang Chen,¹ Rou-Gang Xie,¹ Wei He,¹ Jing Xu,¹ Richard Zhou,¹ Shaoyong Song,¹ Kelsey L. Person,³ Madelyn N. Moore,³ Abigail R. Alwin,³ Ivan Spasojevic,^{4,5} Michael R. Jackson,⁶ Steven H. Olson,⁶ Marc G. Caron,² Lauren M. Slosky,³ William C. Wetsel,^{2,7,8,9} Lawrence S. Barak,² and Ru-Rong Ji^{1,2,9,11,*}

¹Center for Translational Pain Medicine, Department of Anesthesiology, Duke University Medical Center, Durham, NC 27705, USA

²Department of Cell Biology, Duke University Medical Center, Durham, NC 27710, USA

³Department of Pharmacology, University of Minnesota Medical School, Minneapolis, MN 55455, USA

⁴Department of Medicine, Duke University Medical Center, Durham, NC 27710, USA

⁵Pharmacokinetics/Pharmacodynamics Core Laboratory, Duke Cancer Institute, Duke University School of Medicine, Durham, NC 27710, USA

⁶Sanford Burnham Prebys Medical Discovery Institute, La Jolla, CA 92037, USA

⁷Department of Psychiatry and Behavioral Sciences, Duke University Medical Center, Durham, NC 27710, USA

⁸Mouse Behavioral and Neuroendocrine Analysis Core Facility, Duke University Medical Center, Durham, NC 27710, USA

⁹Department of Neurobiology, Duke University Medical Center, Durham, NC 27710, USA

¹⁰These authors contribute equally

¹¹Lead contact

*Correspondence: ru-rong.ji@duke.edu

<https://doi.org/10.1016/j.cell.2025.04.038>

SUMMARY

G-protein-biased agonists have been shown to enhance opioid analgesia by circumventing β -arrestin-2 (β arr2) signaling. We previously reported that SBI-553, a neurotensin receptor 1 (NTSR1)-positive allosteric modulator biased toward β arr2 signaling, attenuates psychostimulant effects in mice. Here, we demonstrate that its analog, SBI-810, exhibits potent antinociceptive properties in rodent models of postoperative pain, inflammatory pain, and neuropathic pain via systemic and local administration. SBI-810's analgesic effects require NTSR1 and β arr2 but not NTSR2 or β arr1. Mechanistically, SBI-810 suppresses excitatory synaptic transmission, inhibits NMDA receptor and extracellular-regulated signal kinase (ERK) signaling in spinal cord nociceptive neurons, reduces Nav1.7 surface expression and action potential firing in primary sensory neurons, and dampens C-fiber responses. Behaviorally, it reduces opioid-induced conditioned place preference, alleviates constipation, and mitigates chronic opioid withdrawal symptoms. These findings highlight NTSR1-biased allosteric modulators as a promising, non-addictive therapeutic strategy for acute and chronic pain management, acting through both peripheral and central mechanisms.

INTRODUCTION

Pain is the leading cause of physician visits, with back pain alone affecting over 600 million people globally. Despite their addictive risks, opioids remain widely prescribed for postoperative and severe pain in the US. Given the substantial economic burden and societal impact of opioid use disorder, federal healthcare agencies have prioritized the development of safer alternatives.¹ Over the past three decades, pain research has focused on targeting ion channels in peripheral sensory neurons, particularly voltage-gated sodium channels Nav1.7 and Nav1.8.^{2–7} Although this approach has achieved notable successes,⁶ the more effective treatments for chronic pain may require targeting both the

peripheral nervous system (PNS) and central nervous system (CNS), given the role of central sensitization in widespread chronic pain.^{8,9} G-protein-coupled receptors (GPCRs) are widely expressed in both the PNS and CNS, offering the largest family for drug targets, including those for analgesics.^{10,11} Beyond opioid receptors,¹² cannabinoid receptors, adenosine receptors, neuropeptide Y (NPY) receptors, orphan GPCRs, and neurotensin (NT) receptors (NTSRs) have been implicated in acute and chronic pain modulation.^{13–17}

NT, a brain-gut tridecapeptide, functions as a neurotransmitter and neuromodulator regulating metabolism, inflammation, mood, and behavior via NT receptor 1/2 (NTSR1/NTSR2).^{18,19} Endogenous NT is found in the spinal cord and

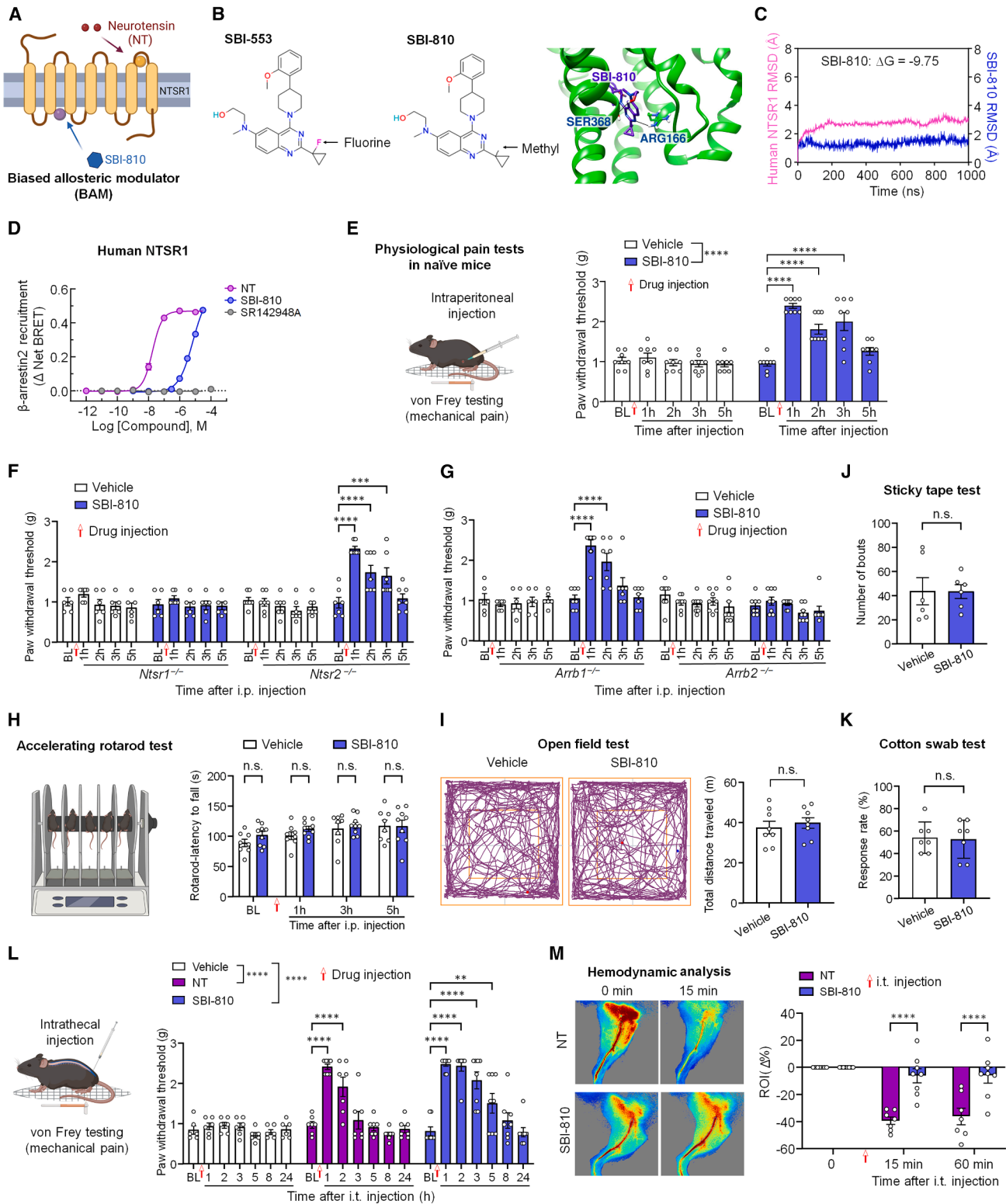


Figure 1. Inhibition of physiological pain by SBI-810 in naive mice through NTSR1 and β arr2

(A) Distinct binding sites on the NTSR1 for NT and SBI-810.

(B) Chemical structures of SBI-553 (left) and SBI-810 (middle) and structural models of hNTSR1 in complex with SBI-810 (right). Key residues are highlighted, including ARG166 and SER368 for hNTSR1. Note the change from fluorine on SBI-553 (left) to the methyl group on SBI-810 (middle).

(legend continued on next page)

dorsal root ganglia (DRGs), and intrathecal (i.t.) NT injection induces potent antinociception.^{20–22} NT analogs targeting NTSR1 and NTSR2 have demonstrated analgesic effects in inflammatory and neuropathic pain models.^{17,23} NT(8–13), the active fragment of NT, is more potent than morphine and produces analgesia in an opioid receptor-independent mechanism.^{24,25} However, NT peptide analogs cause severe side effects, including hypotension and hypothermia, limiting their clinical viability.^{18,26,27}

GPCR activation typically involves G proteins and β -arrestin (β arr) recruitment, leading to receptor desensitization.^{28,29} Structure-based drug design has led to G-protein-biased agonists of μ -opioid receptor (MOR) with reduced side effects. PZM21 selectively activates Gi signaling with minimal β -arrestin-2 (β arr2) recruitment,²⁶ and oliceridine is approved for postoperative pain.²⁷ However, both drugs still cause opioid-associated adverse effects at higher doses.^{28,29} While opioid analgesia is enhanced in β arr2 knockout (KO) (*Arrb2*^{-/-}) mice,³⁰ β arr2 also modulates non-GPCR targets,^{31,32} including pronociceptive NMDA receptors (NMDARs).³³ Since NMDARs regulate spinal cord synaptic plasticity and chronic pain,^{34,35} β arr2 loss can prolong pain in different animal models.³³ Thus, β arr2 activity may complement G protein signaling to mediate analgesia via distinct signaling pathways.

Previously, we characterized the β arr-biased NTSR1 allosteric modulator SBI-553 in rodent addiction models, showing it suppresses psychostimulant-induced locomotion, cocaine self-administration,^{36,37} and alcohol consumption.³⁸ SBI-810, a fluorine to methyl group substitution analog of SBI-553, was designed to improve drug-like properties. We show that SBI-810 provides potent antinociception in mice following intraperitoneal (i.p.) or i.t. administrations. The analgesic effects of SBI-810 require the specific involvement of the NTSR1 and β arr2 signaling. SBI-810 alleviates pain by both peripheral and central mechanisms. Moreover, SBI-810 potentiates acute opioid analgesia and prevents chronic opioid-induced withdrawal responses. Our findings establish β arr2-biased NTSR1 allosteric modulator as a promising and safe therapeutic alternative to opi-

oids for managing acute and chronic pain through both peripheral and central mechanisms.

RESULTS

SBI-810 inhibits acute pain in naive mice through NTSR1 and β arr2

SBI-810 is related to the well-characterized compound SBI-553.³⁹ As a biased allosteric modulator (BAM), SBI-810 binds at a location on the NTSR1 that is different from NT^{36,40} (Figure 1A). SBI-553 and SBI-810 are structurally identical, except for the substitution of the fluorine atom on SBI-553's cyclopropyl ring for a methyl group on SBI-810 (Figure 1B). We investigated interactions of the SBI-810 with the NTSR1 using the solved human structure.³⁶ The strength of the hydrogen bonds between SBI-810 and human NTSR1 was assessed using molecular docking and molecular dynamic simulation (MDS). In the MDS for the human NTSR1-SBI-810 complexes, the root-mean-square deviation (RMSD) value for the protein backbone was stabilized at 1–3 Å (Figure 1C). Simulation analyses revealed a binding energy for SBI-810 ($\Delta G = -9.75$ kcal/mol; Figure 1C). A recent study has revealed SBI-553 interacts with >14 residues on NTSR1.³⁶ By comparison, we found a stronger interaction of ARG166, as well as additional interaction sites with SBI-810 (Figure S1A). Further simulation with mutagenesis of ARG166 to ALA166 resulted both in decreased interactions with SBI-810 (Figures S1B and S1C) and reduced SBI-810-evoked β arr2 recruitment (Figure S1D).

In a bioluminescence resonance energy transfer (BRET) assay assessing β arr2 recruitment to the NTSR1 in HEK293T cells, addition of either NT or SBI-810, but not the NTSR1 antagonist SR142948A, stimulated β arr2 recruitment to the human NTSR1 (Figure 1D). SBI-810 failed to stimulate NTSR1-mediated activation of Gq (Figure S1E, left). Furthermore, SBI-810 antagonized NT-induced Gq activation while promoting NT-induced β arr2 recruitment (Figure S1E, right). NT and SBI-810 also recruited β arr2 through mouse NTSR1 (Figure S1F). Together, these results indicate that SBI-810 is a β arr2 BAM of NTSR1.

(C) Root-mean-square deviation (RMSD) during 1,000 ns simulations of the human NTSR1 (pink) and the NTSR1-SBI-810 complex (blue).

(D) NT- and SBI-810-induced β arr2 recruitment to the human NTSR1. Note that the NTSR1 antagonist SBI-142948A exerted no effects on β arr2 recruitment. Data are presented as the Δ net BRET ratio from 9 independent experiments.

(E) Test for mechanical pain in non-injured mice following vehicle or SBI-810 injection (12 mg/kg, i.p.). Left, schematic of injection and von Frey testing. Right, PWT is showing the effects of vehicle or SBI-810 on mechanical pain ($n = 8$ mice/treatment). SBI-810 induces analgesia as compared with vehicle treatment.

(F) Distinct effects of the vehicle or SBI-810 (12 mg/kg, i.p.) on PWT in *Ntsr1*^{-/-} mice ($n = 6$, left) and *Ntsr2*^{-/-} mice ($n = 7$, right).

(G) Distinct effects of the vehicle or SBI-810 (12 mg/kg, i.p.) on PWT in *Arrb1*^{-/-} mice ($n = 6$ in vehicle treatment, $n = 7$ in SBI-810 treatment, left) and *Arrb2*^{-/-} mice ($n = 8$ per treatment, right).

(H) Rotarod test for drug effects on motor performance. Schematic of the test (left). Latency to fall from the rod at baseline (BL) and 1, 3, and 5 h after vehicle ($n = 8$) or SBI-810 treatment (12 mg/kg, i.p., $n = 9$ mice, right).

(I) Open-field test for drug effects on motor responses. Left, patterns of locomotor activities after vehicle or SBI-810 treatment (12 mg/kg, i.p., $n = 8$ mice). Right, total distance traveled 3 h after treatment.

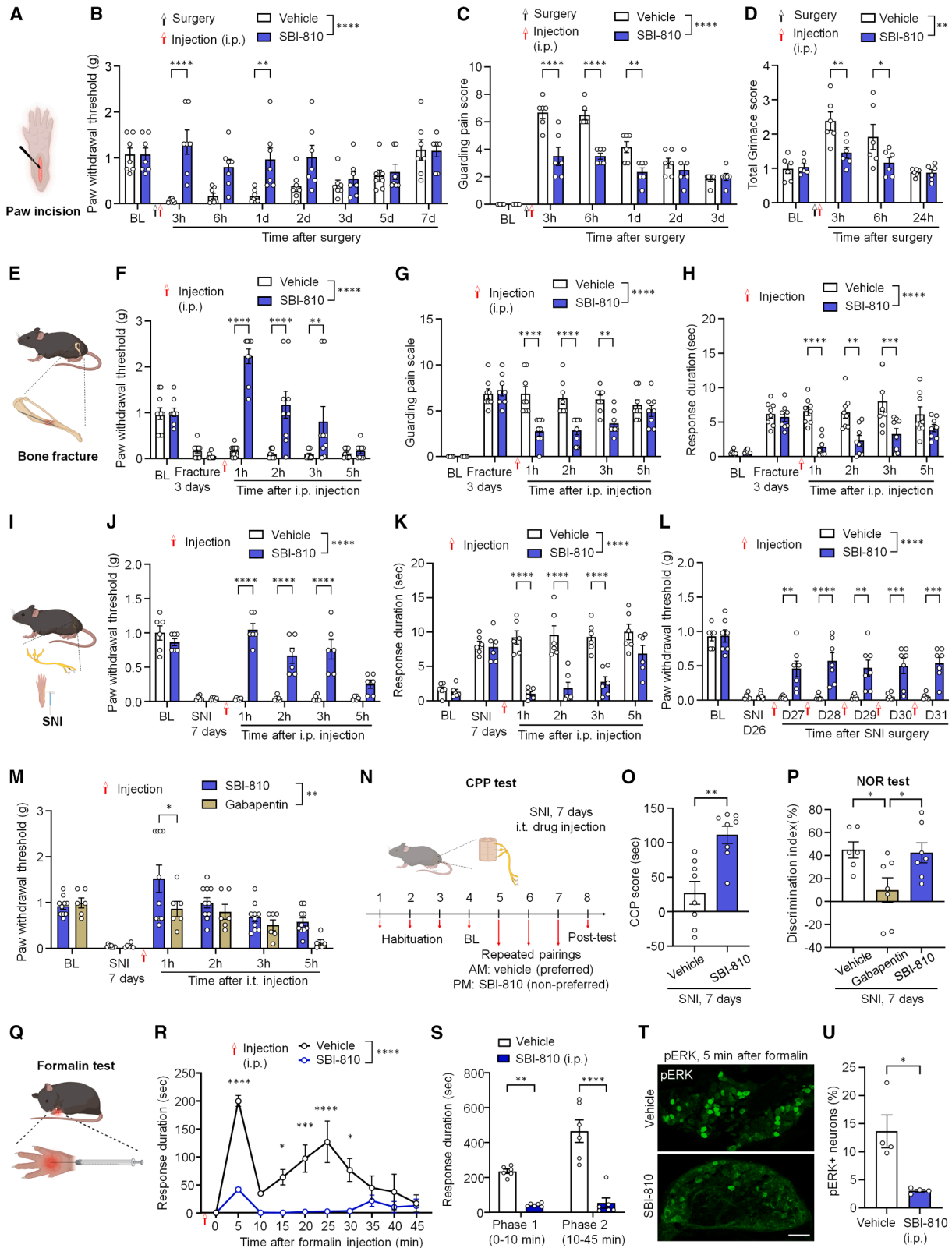
(J and K) Assessment of tactile function in sticky tape test (J, $n = 6$) and cotton swab test (K, $n = 7$), showing no deficit with systemic administration of SBI-810 (12 mg/kg, i.p.).

(L) Left, schematic of intrathecal (i.t.) administration to target the spinal cord/DRG. Right, PWT at BL and 1–24 h after i.t. injection of vehicle ($n = 6$), NT (22 nmol, $n = 7$), or SBI-810 (10 μ g = 22 nmol; $n = 8$ mice/group).

(M) Laser-speckle imaging showing hemodynamic changes in the targeted region of the hind limb in naive mice before and after i.t. injection of NT (22 nmol, $n = 7$) or SBI-810 (22 nmol, $n = 8$).

Data are presented as means \pm SEMs. ** $p < 0.01$, *** $p < 0.001$, **** $p < 0.0001$; ns, not significant. Data were statistically analyzed by unpaired t test (I–K) and two-way repeated-measures (RMs) ANOVA followed by Bonferroni-corrected pairwise comparisons (E–H, L, and M).

See also Figure S1 and Tables S1 and S3 for additional details.



(legend on next page)

To evaluate SBI-810's analgesic effects, we measured paw withdrawal threshold (PWT) using von Frey filaments in naive male and female C57BL/6J mice (Figure 1E, left). We chose a dose of 12 mg/kg (i.p.) based on our previous study with SBI-553.³⁷ SBI-810, but not vehicle, significantly increased PWT within 1 h, with further increases at 2 and 3 h ($p < 0.0001$ vs. vehicle; Figure 1E, right). Thus, SBI-810 effectively inhibits acute pain under basal physiological conditions.

Next, we examined whether SBI-810's analgesic effect depends on NTSR1, NTSR2, β arr1, or β arr2 by testing mutant mice lacking *Ntsr1* or *Ntsr2* and mice with deletion of *Arrb1* or *Arrb2*. SBI-810 increased PWT in *Ntsr2*^{-/-} and *Arrb1*^{-/-} mice but completely lost efficacy in *Ntsr1*^{-/-} and *Arrb2*^{-/-} mice (Figures 1F and 1G). The NTSR1 antagonist SR48692 blocked SBI-810's effect, confirming NTSR1 involvement (Figure S1G). Analgesic responses were consistent across sexes (Figure S1H). SBI-810 also reduced heat and cold pain in hot plate, Hargreaves, and dry ice tests (Figures S1I–S1K) without affecting motor or tactile function in rotarod, open field, sticky tape, and cotton swab tests (Figures 1H–1K). These findings indicate that SBI-810 relieves acute pain via NTSR1 and β arr2 without impairing motor or tactile sensory function.

i.t. drug administration is widely used to evaluate analgesic effects at the spinal cord⁴¹ and DRG.⁴² A single i.t. dose of SBI-810 (10 μ g~22 nmol) or NT (36.8 μ g~22 nmol) significantly increased the PWT at 1–2 h ($p < 0.0001$), with SBI-810 maintaining the effect up to 5 h ($p < 0.01$; Figure 1L). Low doses of NT (0.5 μ g, i.t.) or SBI-810 (1 μ g, i.t.) alone had no effect, but their combination elevated PWT for 2 h ($p < 0.0001$), suggesting a synergistic analgesia (Figure S1N). In the Randall-Selitto test, SBI-810 (20 μ g, i.t.) increased PWT in naive rats (Figure S1O). The spinal analgesia of SBI-810 also required NTSR1 and β arr2 (Figures S1P and S1Q). Furthermore, NT's effect was lost in *Ntsr1*^{-/-} but not *Ntsr2*^{-/-} mice, confirming NTSR1 mediates NT-induced analgesia (Figure S1R).

To further assess potential side effects of SBI-810, we evaluated blood flow using laser-speckle imaging. Unlike NT, which

significantly reduced hind-limb perfusion at 15 and 60 min ($p < 0.0001$), i.t. SBI-810 (22 nmol) had no effect (Figure 1M). Combined with prior tests, our data show that SBI-810 does not impair tactile sensation, motor function, or blood flow.

To determine the concentrations of SBI-810 in the brain, spinal cord, and DRG following i.t. administration, we conducted pharmacokinetic studies by collecting these tissues between 0.25 and 24 h after administration. We found that SBI-810 concentrations in DRG were higher than those in spinal cord and much higher than in brain at 0.25, 0.5, 1, 2, and 4 h (Figure S1S). Therefore, the spinal cord and DRG are key sites of SBI-810's analgesic action via i.t. delivery.

Systemic or local treatment of SBI-810 mitigates postoperative, neuropathic, and inflammatory pain

The G-protein-biased opioid receptor agonist oliceridine was approved for in-patient management of postoperative pain.⁴³ We compared the analgesic effects of SBI-810 and oliceridine using a mouse model of plantar incision-induced postoperative pain (Figure 2A).⁴⁴ Following plantar incision, mechanical pain developed within 3 h and recovered within 7 days in vehicle-treated mice. Systemic treatment of SBI-810 (12 mg/kg, i.p.) prevented the incision-induced mechanical pain (Figure 2B). Plantar incision also produced spontaneous pain on the first day, as assessed by guarding behavior and facial expression using the Grimace scale,^{45,46} while SBI-810 blocked these behaviors (Figures 2C and 2D). In another pain model, tibial fracture results in severe and persistent postoperative pain⁴⁷ (Figures 2E–2H). Notably, SBI-810 effectively alleviated mechanical, spontaneous, and cold pain in this fracture model (Figures 2F–2H).

The spared nerve injury (SNI) model (Figure 2I) is one of the most extensively used animal models of neuropathic pain.⁴⁸ SNI leads to drastic mechanical and cold pain in mice, and both were reversed by SBI-810 (12 mg/kg, i.p.) administered 1 week post-injury (Figures 2J and 2K). These analgesic actions were completely lost in *Ntsr1*^{-/-} (Figures S2A–S2C) and *Arrb2*^{-/-} mice with SNI (Figures S2D–S2F).

Figure 2. Systemic and local administration of SBI-810 reduces postoperative, neuropathic, and inflammatory pain in mice

(A–D) Postoperative pain after plantar incision. (A) Schematic of plantar incision in a hind paw. (B–D) Incision-induced mechanical pain (B), spontaneous pain (C, guarding behavior), and facial expression of pain (D, Grimace scale) after systemic administration of vehicle or SBI-810 (12 mg/kg, i.p.) immediately after incision. $n = 7$ in (B); $n = 6$ in (C) and (D).

(E–H) Postoperative pain after tibial fracture. (E) Schematic of tibial bone fracture in a hind limb. (F–H) Fracture-induced mechanical pain (F), spontaneous pain (G, guarding behavior), and cold pain (H, response duration in acetone test) following systemic injection (i.p.) of vehicle or SBI-810 (12 mg/kg, i.p.). $n = 10$ (vehicle) and $n = 9$ (SBI-810) in (F); $n = 8$ in (G) and (H).

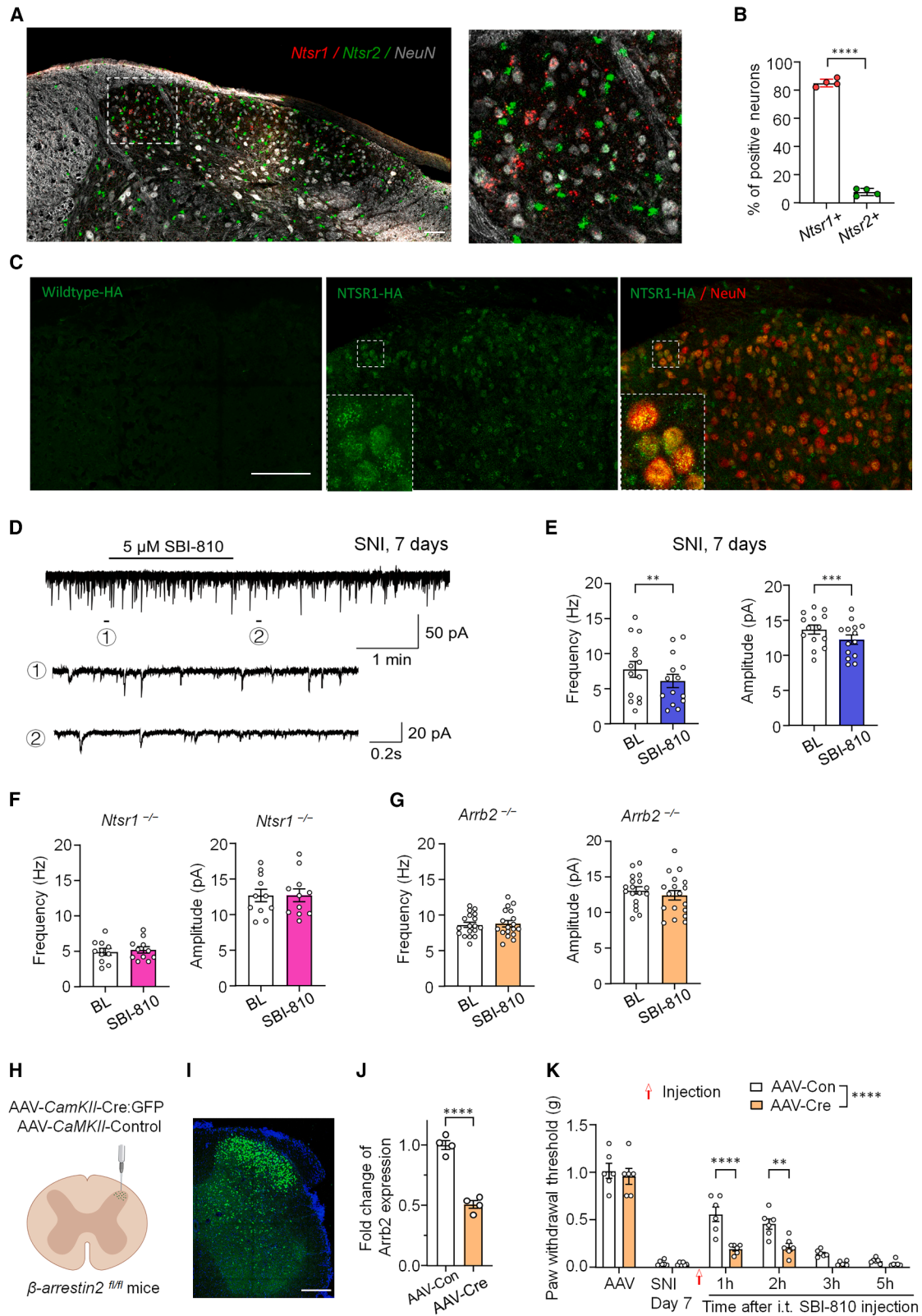
(I–P) Neuropathic pain after spared nerve injury (SNI). (I) Schematic of SNI in a hind limb. (J and K) SNI-induced mechanical pain (J) and cold pain (K, response duration in acetone test) following systemic administration of vehicle or SBI-810 (12 mg/kg, i.p.). $n = 6$. (L) Analgesic effects of repeated injections of SBI-810 (12 mg/kg, i.p.) on mechanical pain in SNI mice following daily injections. PWT was tested 1 h after each injection. $n = 6$ (vehicle), $n = 7$ (SBI-810). (M) Comparison of SBI-810 (10 μ g, i.t., $n = 10$) with gabapentin (10 μ g, i.t., $n = 6$) for their abilities to inhibit SNI-induced mechanical pain. (N and O) Schematic of CPP test for assessing SNI-induced spontaneous pain in vehicle and SBI-810 (10 μ g, i.t.) treated mice (N). (O) CPP score in SNI mice ($n = 8$). (P) Novel object recognition (NOR) memory test conducted 30 min post-administration showing cognitive impairment by gabapentin (10 μ g, i.t., $n = 7$) but not SBI-810 (10 μ g, i.t., $n = 7$). $n = 6$ (vehicle).

(Q–S) Formalin (5%) induced inflammatory pain. (Q) Schematic of intraplantar injection of formalin. (R) Time course of spontaneous pain (flinching/licking/flicking) following vehicle ($n = 6$) or SBI-810 ($n = 6$, 12 mg/kg, i.p.) treatment. (S) Duration of spontaneous pain in phase 1 (0–10 min) and phase 2 (10–45 min).

(T and U) SBI-810 inhibits formalin-induced pERK in DRG neurons at 5 min. (T) pERK photographs in DRG neurons from formalin-injected mice pre-treated with vehicle or SBI-810 (12 mg/kg, i.p.). Scale bar, 100 μ m. (U) Quantification of the percentage of pERK+ neurons ($n = 4$ mice/treatment).

Data are represented as means \pm SEMs. Mice from both sexes were tested. Black arrows indicate surgery, and red arrows indicate drug injection. * $p < 0.05$, ** $p < 0.01$, *** $p < 0.001$, **** $p < 0.0001$. Data were statistically analyzed by unpaired t test (O and U), one-way ANOVA (P), and two-way RM-ANOVA followed by Bonferroni post hoc comparisons (B–D, F–H, J–M, R, and S).

See also Figure S2 and Table S1 for additional details.



(legend on next page)

Unlike morphine, which induces tolerance with repeated use,⁴⁹ daily SBI-810 injections (12 mg/kg, i.p.) for 5 days during late-phase SNI (4 weeks) maintained stable analgesia without tolerance or sensitization (Figures 2L and S2G). Additionally, we evaluated SBI-810 against gabapentin, a frequently prescribed medication for neuropathic pain.⁵⁰ i.t. SBI-810 was more effective at reducing SNI-induced mechanical pain ($p < 0.01$; Figure 2M), and systemic SBI-810 also showed greater efficacy (Figures S2H and S2I). Importantly, SBI-810 (10 μ g, i.t.) did not cause gabapentin-like side effects such as sedation (Figures S2J and S2K). Conditioned place preference (CPP) has been widely used to assess ongoing neuropathic pain in animals.⁵¹ In CPP assays, SBI-810 produced robust preference in SNI-injured mice, indicating relief of ongoing pain (Figures 2N and 2O). SBI-810 also reduced mechanical pain in the Randall-Selitto test (Figure S2L) and, unlike gabapentin, did not impair cognition in the novel object recognition test (Figure 2P).

The G-protein-biased opioid agonist oliceridine (TRV130) has been found to be more potent than morphine in the tail-flick assay, and it produced pain relief in a bone fracture model following i.p. administration.⁵² We compared the analgesic efficacy of oliceridine and SBI-810 following i.t. injections (22 nmol). Both showed similar increases in the PWT in naive animals (Figure S2M). However, in the bone fracture model, SBI-810 exhibited greater inhibition of mechanical pain (Figure S2N), and mice displayed less guarding behavior than mice treated with oliceridine (Figures S2O).

We further tested SBI-810 in additional animal models of inflammatory pain and neuropathic pain, induced by complete Freund's adjuvant (CFA), streptozotocin (STZ, a diabetes model), and formalin. Systemic SBI-810 reduced mechanical and thermal pain in CFA and STZ models (Figures S2P–S2S). In the formalin test, spontaneous pain during phase 1 (0–10 min) and phase 2 (10–45 min) reflects peripheral and central sensitization, respectively.^{53,54} Notably, systemic SBI-810 inhibited phase 1 responses ($p < 0.01$, Figures 2Q–2S), indicating peripheral modulation. Additionally, this treatment reduced formalin-induced nociceptor activation in DRG neurons, as revealed by phosphorylation levels of extracellular-regulated signal kinase (pERK), a marker for nociceptor activation,⁵⁵ 5 min post-formalin injection ($p < 0.05$; Figures 2T and 2U),

further supporting SBI-810's peripheral regulatory role. SBI-810 also significantly mitigated phase 2 responses ($p < 0.0001$, Figures 2Q–2S), highlighting its central effects. Collectively, these findings demonstrate SBI-810 effectively alleviates post-operative, inflammatory, and neuropathic pain through both peripheral and central mechanisms.

Central modulation of spinal cord neural plasticity by SBI-810

Chronic pain involves both central sensitization (altered spinal synaptic transmission) and peripheral sensitization (increased sensory neuron excitability/sensitization).^{34,56–58} To explore SBI-810's central mechanisms, we examined NTSR1 and NTSR2 expression in the spinal cord dorsal horn (SDH) that is crucial for pain modulation.^{59,60} *In situ* hybridization with RNAscope probes revealed non-overlapping patterns: *Ntsr1* mRNA localized to NeuN-positive cells (neurons), whereas *Ntsr2* mRNA was in NeuN-negative cells (Figures 3A and 3B). Double immunostaining in *Ntsr1*-hemagglutinin (HA) reporter mice confirmed the colocalization of NTSR1 and NeuN in SDH neurons (Figure 3C). To ascertain the function of SBI-810 in modulating nociceptive synaptic transmission, spontaneous excitatory postsynaptic currents (sEPSCs) were recorded in lamina II neurons from spinal cord slices obtained from SNI mice (Figures 3D and 3E). Perfusion of spinal cord slices with SBI-810 (5 μ M) reduced the frequency and amplitude of the sEPSCs in these neurons (Figure 3E). Notably, SBI-810 failed to alter the frequency and amplitude of the sEPSCs in *Ntsr1*^{−/−} and *Arb2*^{−/−} mice (Figures 3F, 3G, and S3A–S3F).

β arr2 is widely expressed in both excitatory and inhibitory neurons in SDH.³³ To examine the role of β arr2 in SDH excitatory neurons, we employed an adeno-associated virus (AAV) approach to selectively delete *Arb2* in ipsilateral CaMKII+ excitatory neurons via intra-SDH microinjection³³ (Figure 3H). This approach led to targeted AAV expression in the ipsilateral SDH 3 weeks post-microinjection (Figure 3I) and effective *Arb2* knockdown in the same region (Figure 3J). Notably, the ability of SBI-810 to suppress SNI-induced mechanical pain was diminished after *Arb2* deletion using AAV-Cre expression in SDH of *Arb2*-floxed mice (Figure 3K).

NMDARs are pivotal in driving spinal cord synaptic plasticity and chronic pain,^{33–35} partly through pERK.⁵³ i.t. injection of

Figure 3. Central action of SBI-810 by inhibition of spinal cord synaptic transmission via NTSR1 and β arr2 in mice

(A and B) Distinct expression of *Ntsr1* and *Ntsr2* mRNAs in SDH. (A) Triple staining of *in situ* hybridization with RNAscope probes for *Ntsr1* mRNA (red) and *Ntsr2* mRNA (green), and immunostaining for NeuN (gray) in SDH (left). Enlargement from the boxed area (right). Note non-overlapping expression of *Ntsr1* and *Ntsr2* in neurons and non-neuronal cells. Scale bar, 50 μ m. (B) Percentage of *Ntsr1* and *Ntsr2* mRNAs in NeuN+ neurons ($n = 4$ mice).

(C) NTSR1 expression in SDH neurons in NTSR1-HA reporter mice. Left and middle, single staining of NTSR1/HA in control WT and NTSR1-HA reporter mice. Right, double immunostaining in NTSR1-HA reporter mice showing the colocalization of the NTSR1 and NeuN in SDH neurons. The small boxes are enlarged. Scale bar, 100 μ m (left).

(D–G) SBI-810 inhibits excitatory synaptic transmission in SDH neurons via NTSR1 and β arr2. (D) Representative traces of sEPSCs in lamina II neurons in spinal cord before (1) and 2 min of SBI-810 (5 μ M) perfusion (2). sEPSC recordings were conducted in spinal cord slices collected from SNI mice. (E) Frequency and amplitude of sEPSCs showing the inhibitory effects of SBI-810 in SNI mice ($n = 14$ neurons from 4 mice). BL, baseline. (F and G) SBI-810 exerts no effects on sEPSC frequency and amplitude in lamina II neurons from *Ntsr1*^{−/−} (F, $n = 11$ neurons from 4 mice) or *Arb2*^{−/−} mice (G, $n = 18$ neurons from 4 mice).

(H–K) β arr2 in spinal cord excitatory neurons mediates SBI-810's antinociceptive effect in SNI mice. (H) Schematic of intra-spinal cord microinjection of AAV vectors into *Arb2*^{flox/flox} mice. (I) Specific expression of AAV-CamKII-Cre-GFP in excitatory neurons in superficial SDH of *Arb2*^{flox/flox} mice. Scale bar, 200 μ m. (J) Fold change of *Arb2* mRNA expression (shown by RT-qPCR) after spinal microinjection of control AAV-Cre or AAV-control (Con). $n = 4$. (K) SNI-induced mechanical pain following SBI-810 (10 μ g, i.t.) in *Arb2*-floxed mice treated with AAV ($n = 6$).

Data are shown as means \pm SEMs. Mice from both sexes were included. Red arrow indicates drug injection. ** $p < 0.01$, *** $p < 0.001$, **** $p < 0.0001$. Data were statistically analyzed by unpaired t test (B and J), paired t tests (E–G), and two-way RM-ANOVA followed by Bonferroni post hoc comparisons (K).

See also Figure S3 and Table S1 for additional details.

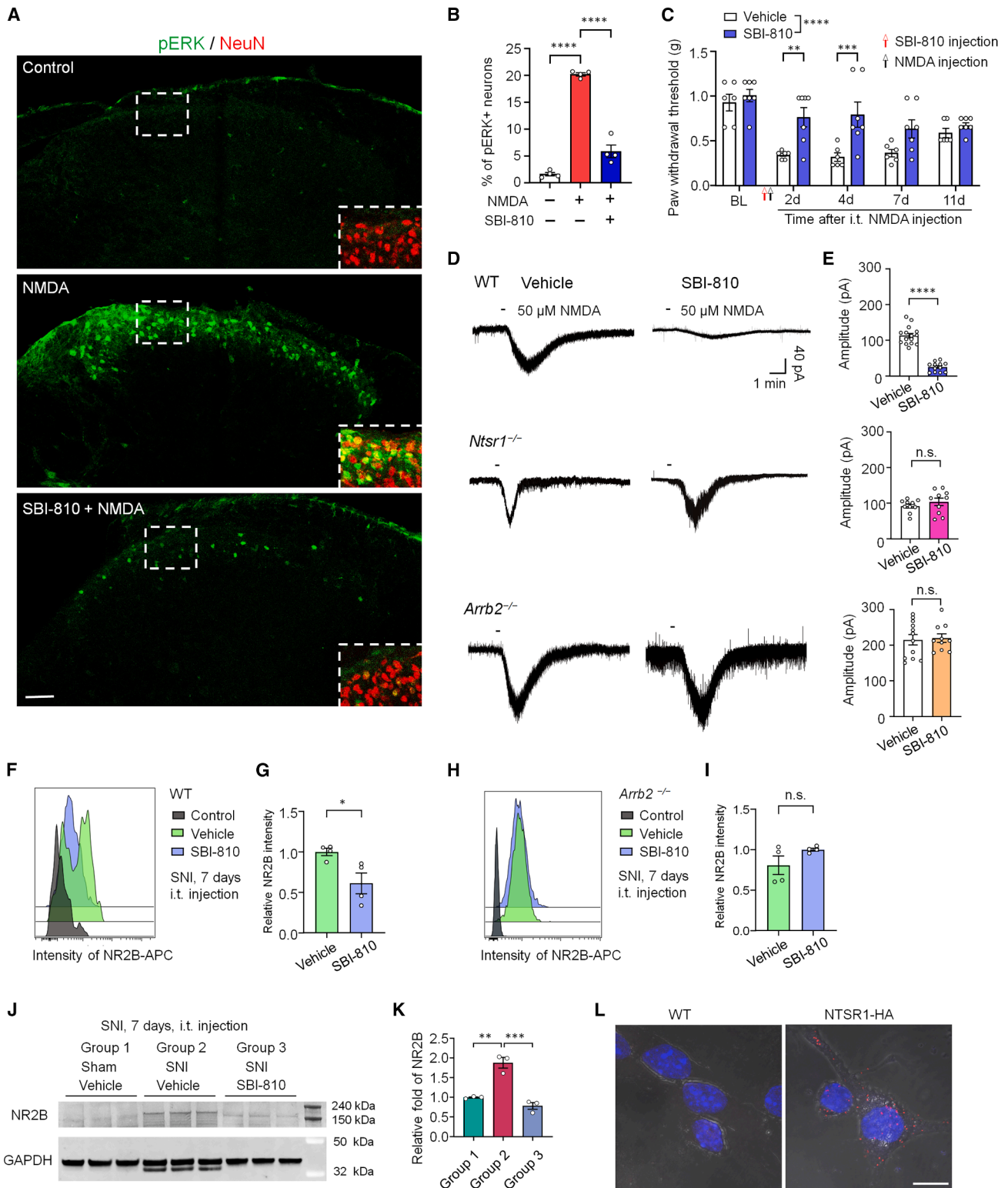


Figure 4. Central action of SBI-810 by inhibition of NMDARs and ERK activation in spinal cord neurons via NTSR1 and β arr2

(A and B) SBI-810 inhibits NMDA-induced ERK activation in SDH neurons. (A) Photographs of double immunostaining of pERK (green) and NeuN (red) in SDH from mice 10 min after NMDA administration (i.t., 1 nmol). Scale bar, 50 μ m. (B) Quantification of the percentage of pERK+ neurons ($n = 4$). (C) PWT following i.t. injection of NMDA (1 nmol) with vehicle ($n = 6$) or SBI-810 (10 μ g, $n = 7$).

(legend continued on next page)

NMDA (1 nmol) significantly increased pERK expression selectively in NeuN+ neurons ($p < 0.0001$) in the superficial SDH (laminae I-II), a key area for pain processing.⁵⁹ However, this pERK increase was largely prevented by i.t. SBI-810 treatment ($p < 0.0001$; Figures 4A and 4B). Additionally, the same i.t. NMDA injection induced mechanical allodynia for over 7 days, which was effectively prevented by SBI-810 (Figure 4C). Patch-clamp studies on spinal cord slices revealed that bath application of NMDA (50 μ M) elicited inward currents in lamina II neurons, which were significantly depressed by SBI-810 perfusion in wild-type (WT) mice ($p < 0.0001$; Figures 4D and 4E). However, this inhibitory effect was not observed in *Ntsr1*^{-/-} mice (Figures 4D and 4E). Furthermore, while NMDA-induced currents nearly doubled in *Arrb2*^{-/-} mice vs. WT mice (~ 200 vs. ~ 100 pA), SBI-810 did not alter the currents in these mutants (Figures 4D and 4E), thereby confirming β arr2 plays a crucial role in mediating the effects of SBI-810.

Mechanistically, we tested the involvement of ERK in β arr2's regulation of NMDAR function using the NMDAR antagonists (TCN201 for GluN2A/NR2A and Ro 25-6981 for GluN2B/NR2B³³) and the ERK kinase (MEK1/2) inhibitor U0126. Perfusion of spinal cord slices with 50 μ M NMDA induced a rapid (<10 min) and persistent (>120 min) increase in pERK in superficial SDH neurons (NeuN+) of WT mice, peaking at 30 min (Figures S4A and S4B). NMDA induced significantly greater neuronal pERK expression in *Arrb2*^{-/-} mice at different time points (30–120 min) relative to their WT controls (Figure S4B). Furthermore, NMDA-induced pERK from both WT and *Arrb2*^{-/-} mice was partially reduced by the GluN2A antagonist TCN201 and blocked by the GluN2B antagonist Ro 25-6981 (Figures S4C and S4D), suggesting that GluN2B subunits play a greater role than GluN2A subunits in regulating NMDA-induced ERK activation in SDH neurons. Additional patch-clamp recordings revealed ERK inhibition with U0126 exerted no significant effect on NMDA-induced currents in WT neurons ($p > 0.05$), but it completely blocked the increase of NMDA currents in spinal neurons of *Arrb2*^{-/-} mice ($p < 0.05$; Figures S4E and S4F). Additionally, i.t. NMDA-induced spontaneous pain was significantly increased in *Arrb2*^{-/-} compared with WT mice ($p < 0.05$), and this spontaneous pain was blocked by U0126 in both WT and *Arrb2*^{-/-} mice (Figure S4G). These findings highlight a crosstalk among NMDAR, ERK, and β arr2 in central sensitization.

Given the crucial role of β arr2 in receptor trafficking/internalization, we investigated whether SBI-810 affects the surface expression of GluN2B/NR2B in SDH using fluorescence-activated cell sorting (FACS) analysis using an antibody that

recognizes the extracellular domain of NR2B. i.t. treatment with SBI-810 significantly reduced surface NR2B expression at 1 h ($p < 0.01$; Figures 4F and 4G). Notably, this inhibitory effect of SBI-810 was absent in *Arrb2*^{-/-} mice (Figures 4H and 4I). Western blot analysis confirmed a significant increase in NR2B in the SDH after SNI ($p < 0.01$), which was significantly reduced by i.t. SBI-810 treatment ($p < 0.001$; Figures 4J and 4K). Conversely, i.t. SBI-810 did not alter the expression of AMPA receptor subunits GluNA1 and GluNA2 in SDH (Figures S4H–S4K).

To examine the potential interaction of NTSR1 with NR2B, we performed a proximity ligation assay (PLA)⁶¹ on dissociated spinal cord neurons. We found puncta-like signals in cell bodies close to the surface and in dendrites (Figure 4L), suggesting a close colocalization of NTSR1 with NR2B. Taken together, these results indicate that modulation of synaptic transmission, NMDAR surface expression and function, and ERK activation in spinal cord nociceptive neurons are key mechanisms through which SBI-810 attenuates pain through β arr2-mediated signaling from NTSR1.

Peripheral modulation of nociceptor excitability by SBI-810

Nerve injury has been shown to upregulate NT and its receptors in DRG neurons and the lumbar spinal cord.²² Electrophysiological studies revealed the presence of NT-responsive neurons in DRG cultures.^{62,63} We used both *in vivo* (Figures 5A–5D) and *in vitro* (Figures 5E–5G) electrophysiological recordings to investigate the effects of SBI-810 on nociceptor activity. When painful C-fiber activity was induced with footpad stimulation in anesthetized mice, sensory-motor reflexes were recorded from the biceps femoris muscle via electromyographic (EMG) recordings (Figure 5A). Compared with naive WT and *Ntsr1*^{-/-} mice, animals with bone fractures exhibited heightened C-fiber responses regardless of genotype, showing increases in frequency, amplitude, and duration but decreases in latency in evoked C-fiber responses (Figures 5B–5D and S5A–S5G). Local peri-sciatic administration of SBI-810 (10 μ g) resulted in rapid (≤ 5 min) and significant inhibition ($p < 0.0001$) of both the amplitude and frequency of C-fiber responses in WT mice undergoing bone fracture surgery (Figures 5B–5D). SBI-810 also rapidly (within 5 min) increased the latency and reduced the duration of C-fiber responses only in WT animals (Figures S5A and S5B). Additionally, SBI-810 altered the frequency, latency, amplitude, and duration of C-fiber responses in naive WT mice without injury (Figures S5C–S5G). However, all of these SBI-810-mediated effects were completely lost in injured *Ntsr1*^{-/-} mice (Figures 5B–5D and S5A–S5G). These *in vivo*

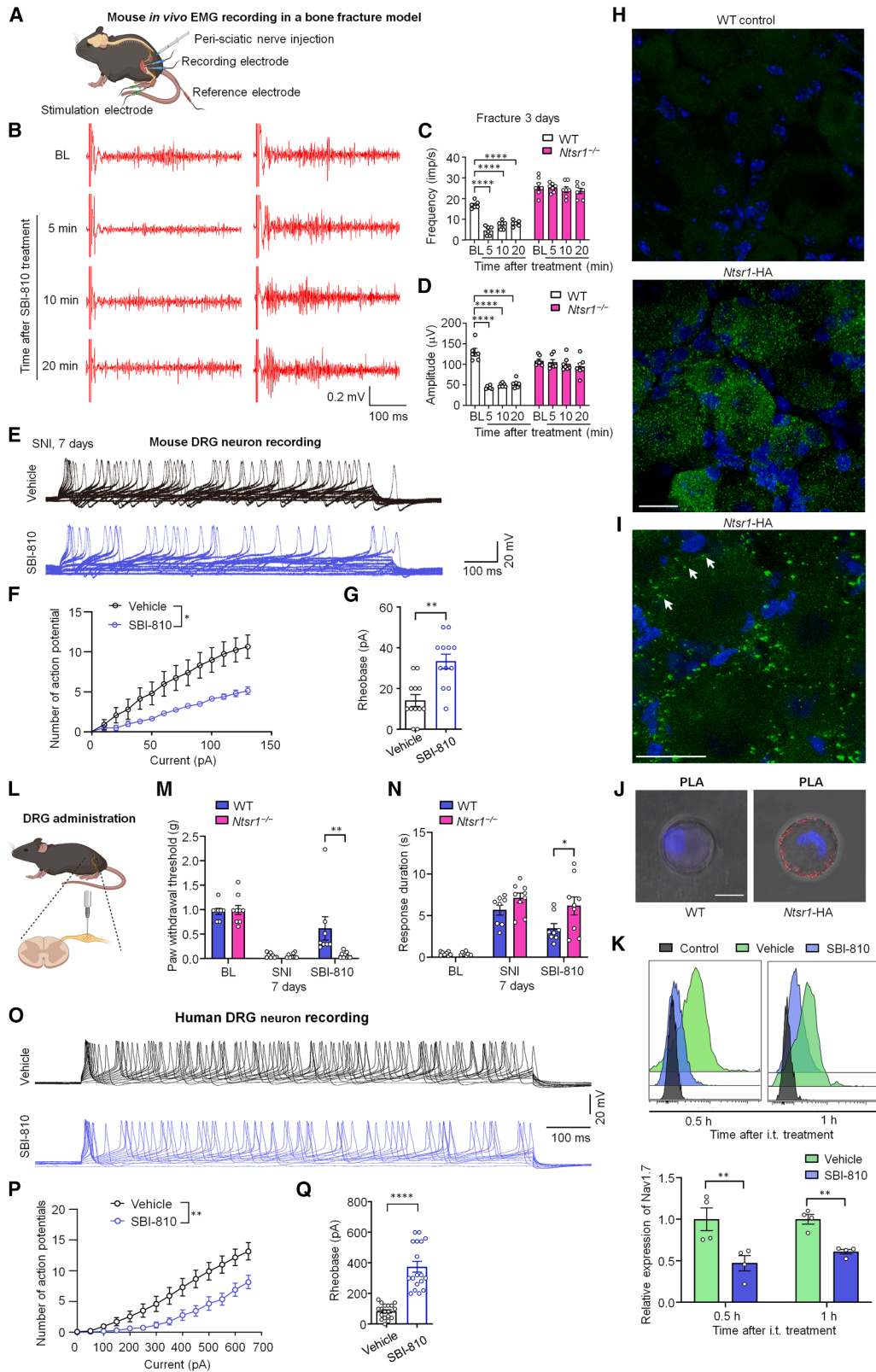
(D and E) SBI-810 inhibits NMDA-induced currents in SDH neurons of spinal cord slices via NTSR1 and β arr2. (D) Representative traces of NMDA (50 μ M)-induced inward currents in lamina II neurons from WT, *Ntsr1*^{-/-}, or *Arrb2*^{-/-} mice with the blocking effects of SBI-810 (5 μ M) compared with vehicle. (E) Amplitude of NMDA-induced currents in spinal cord slices with vehicle or SBI-810 (5 μ M) treatment in three genotypes of mice. $n = 10$ –15 neurons from 5 to 9 mice.

(F–I) FACS analysis showing the surface expression of the GluN2B subunit in SDH following i.t. treatment with vehicle or SBI-810 (10 μ g) in WT (F and G) and *Arrb2*^{-/-} mice (H and I). Graphs show cell distribution (F and H) and relative intensities (G and I) of GluN2B signal ($n = 4$).

(J–L) Western blot analysis showing GluN2B expression in SDH and the effects of SNI with vehicle and SBI-810 (10 μ g, i.t.) treatments in WT mice. (J) Western gels immunolabeled by GluN2B and GAPDH (load control). (K) Quantification of relative intensities of the GluN2B signal ($n = 3$). (L) Proximity ligation assay (PLA) showing NTSR1-NR2B interaction in dissociated spinal cord neurons. Scale bar, 10 μ m.

Data depicted as means \pm SEMs. Mice from both sexes were included. Red and black arrows indicate drug injection. * $p < 0.05$, ** $p < 0.01$, *** $p < 0.001$, **** $p < 0.0001$, n.s., not significant. Data were statistically analyzed by unpaired t tests (E, G, and I), one-way ANOVA (B and K), and two-way RM-ANOVA (C), followed by Bonferroni post hoc comparisons.

See also Figure S4 and Table S1 for additional details.



(legend on next page)

electrophysiology studies indicate rapid and local effects of SBI-810 in suppressing C-fiber-induced nociceptive responses in WT mice, but these effects are absent in *Ntsr1*^{-/-} mutants.

To validate the direct action of SBI-810 in sensory neurons, we recorded action potentials (APs) in dissociated small-sized neurons (presumably nociceptors) in primary cultures from mouse DRG. SBI-810 (5 μ M) significantly reduced the firing rates of APs and increased the rheobase for AP induction ($p < 0.05$, Figures 5E–5G). To prove the critical involvement of NTSR1, we demonstrated that SBI-810's effects were abolished in the DRG neurons of *Ntsr1*^{-/-} mice (Figures S5H–S5J).

Investigation of the cellular localization of NTSR1 was assessed in DRG neurons. Anti-HA tag immunostaining revealed punctate staining in mouse DRG neurons of reporter mice but not in littermate control WT mice (Figure 5H). High-magnification confocal microscopy imaging showed labeled punctuates near the surface of DRG neurons in NTSR1-HA reporter mice (Figure 5I).

The TTX-sensitive sodium channel subtype Nav1.7 is highly expressed in mouse and human DRG neurons and plays a critical role in evoking APs in sensory neurons.⁷ PLA revealed specific signals on the surface of DRG neurons, suggesting a close membrane colocalization of the NTSR1 with Nav1.7 (Figure 5J). Furthermore, the PLA result showed a significant decrease ($p < 0.05$) in surface signaling in DRG neurons treated with SBI-810 (Figures S5K and S5L). FACS analysis showed significant reductions in Nav1.7 surface expression in DRG neurons at 0.5 and 1 h following i.t. SBI-810 treatment ($p < 0.01$; Figure 5K). By contrast, i.t. SBI-810 did not alter the expression of Nav1.7 in *Ntsr1*^{-/-} and *Arrb2*^{-/-} mice (Figures S5M and S5N). These results suggest the formation of a possible NTSR1- β arr2-Nav1.7 complex near the surface of DRG neurons. We also postulate that treatment with SBI-810 may cause Nav1.7 internalization via β arr2.

To further validate that SBI-810's inhibition of sensory neuronal activity can effectively reduce pain, we directly administered SBI-810 (2 μ g) to the lumbar DRG by microinjection (Figure 5L).¹⁴ The intra-ganglionic injection reduced both mechanical pain (Figure 5M) and cold pain (Figure 5N) in WT but not in *Ntsr1*^{-/-} mice undergoing SNI surgery. Combined with

the analgesic effects observed following peri-sciatic administration of SBI-810, our results strongly indicate that SBI-810 modulates pain through peripheral mechanisms.

Dysregulation of Nav1.7 by NEDD4 E3 ubiquitin ligase in DRG neurons contributes to neuropathic pain.^{64–66} β arr2 can recruit E3 ligases like MDM2 and NEDD4 to promote ubiquitination and sustained intracellular signaling.^{67,68} Using a DRG pull-down assay, we found that SBI-810 significantly increased Nav1.7 ubiquitination ($p < 0.01$; Figure S5O). Furthermore, the ubiquitination inhibitors MG132 and epoxomicin prevented the SBI-810-induced antinociceptive effects in NMDA-induced pain models (Figure S5P), indicating a key role for ubiquitination in SBI-810-mediated analgesia.

Endosomal GPCR signaling, such as via neurokinin 1, drives sustained nociception.⁶⁹ Notably, endosome inhibitors Dy4 and PS2 blocked SBI-810's antinociceptive effects (Figure S5Q). Both Dy4 and the ubiquitination inhibitor MG132 prevented SBI-810's suppression of NMDA-induced mechanical pain (Figure S4L). Additionally, MG132 blocked the SBI-810-induced reduction of sEPSC in SDH neurons from SNI mice (Figures S3G–S3J), underscoring the importance of ubiquitination and endosomal signaling in SBI-810's analgesic mechanism.

The effective translation of preclinical analgesics is frequently limited by species differences in human and mouse nociceptors.^{70,71} To address this issue, we assessed SBI-810's effects on human DRG neuron cultures prepared by tissue donors. We performed patch-clamp recordings on small-diameter neurons (<50 μ m)⁷² and observed a significant inhibition of AP firing by SBI-810 (5 μ M, $p < 0.01$; Figures 5O and 5P). Additionally, SBI-810 increased the rheobase, thereby reducing the excitability of human DRG neurons ($p < 0.0001$; Figure 5Q). Thus, SBI-810's inhibitory effects on AP firing and neuronal excitability are fully retained in human DRG nociceptive neurons.

SBI-810 enhances opioid analgesia and reduces tolerance and withdrawal

The endogenous opioid system is pivotal in nociception.¹² We investigated the role of opioid receptors in SBI-810's antinociceptive actions using the tail-flick and hot-plate tests, where

Figure 5. Peripheral action of SBI-810 occurs through inhibition of C-fiber responses and neuronal excitability

(A–D) EMG recordings in biceps femoris muscle in mice with bone fracture. (A) Schematic of EMG. C-fiber activity was induced in anesthetized mice by stimulating the footpad and recording the sensory-motor reflex. (B) Representative EMG traces following C-fiber stimulation at BL and then at 5, 10, and 20 min post-drug treatment (peri-sciatic) in *Ntsr1*^{-/-} mice and WT littermate controls. (C and D) EMG frequency (C) and amplitude (D) in WT mice ($n = 6$) and *Ntsr1*^{-/-} mice ($n = 7$).

(E–G) Patch-clamp recordings in dissociated mouse DRG neurons with small diameters (<25 μ m) from WT mice. (E) Representative traces of evoked APs and effects of SBI-810 (5 μ M). (F and G) Quantification of the firing rate of APs (F) and rheobase (G). $n = 12$ neurons from 4 mice.

(H and I) NTSR1 expression, labeled with an anti-HA antibody, in dissociated DRG neurons from NTSR1-HA reporter mice and control mice, with confocal imaging (H) and high-resolution imaging (63 \times , oil, I). Arrows indicate possible surface expression of NTSR1. Scale bar, 20 μ m.

(J) PLA showing colocalization of Nav1.7 and NTSR1 (labeled with anti-HA antibody). Scale bar, 10 μ m.

(K) FACS analysis showing the surface expression of Nav1.7 in the DRG following vehicle or SBI-810 (10 μ g, i.t.) treatments in WT mice. Top, cell distribution. Bottom, relative expression of Nav1.7 signal. $n = 4$.

(L–N) Behavioral testing in the SNI model following intra-ganglion microinjection. (L) Schematic of intra-ganglion microinjection in L4–L5 DRG. (M and N) DRG microinjection of SBI-810 (2 μ g) reduced SNI-induced mechanical pain (M) and cold pain (N) in WT, but not in *Ntsr1*^{-/-} mice. $n = 8–9$ mice.

(O–Q) Patch-clamp recordings in dissociated human DRG neurons with small diameters (<50 μ m). (O) Traces of evoked APs and effects of SBI-810 (5 μ M) in human DRG neurons. (P and Q) Quantification of AP firing rate (P) and rheobase (Q) in human DRG neurons. $n = 18–20$ neurons from 5 donors.

Data are presented as means \pm SEMs. Mice from both sexes were included. Unpaired t test (G and Q), two-way ANOVA (K), and two-way RM-ANOVA (C, D, F, M, N, and P), followed by Bonferroni post hoc comparisons. * $p < 0.05$, ** $p < 0.01$, **** $p < 0.0001$, as indicated.

See also Figure S5 and Table S1 for additional details.

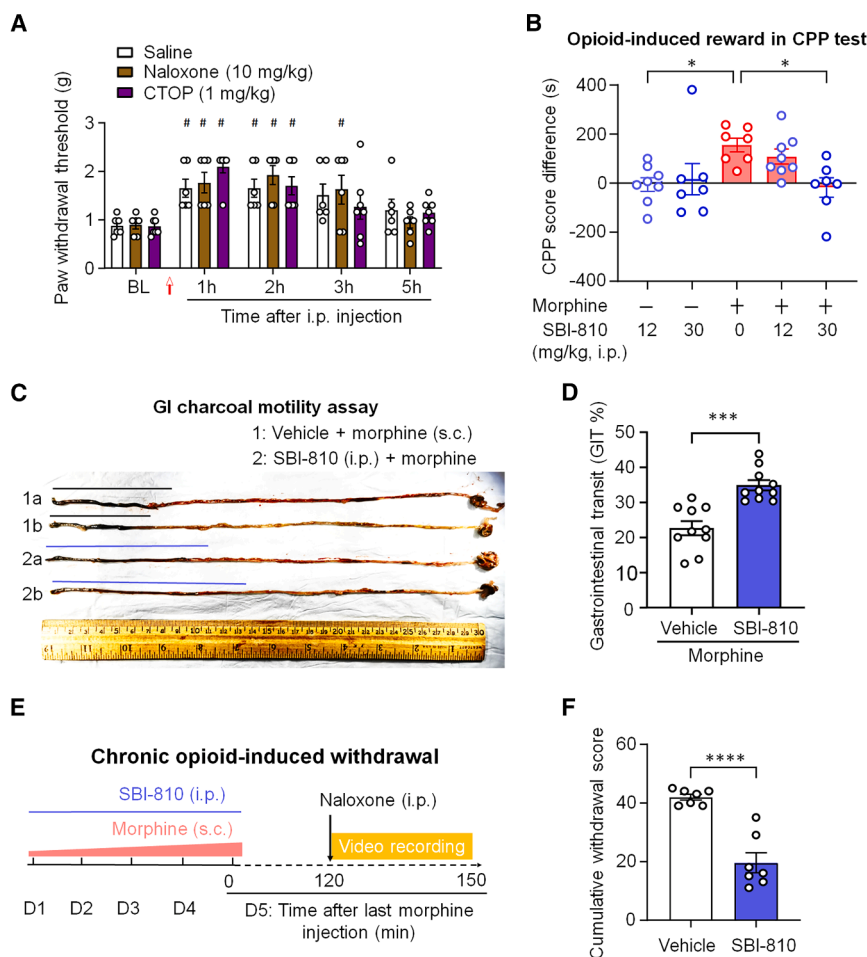


Figure 6. Inhibition of acute opioid-induced reward and constipation and chronic opioid-induced withdrawal by SBI-810 in mice

(A) von Frey test showing the effects of i.p. injection of the opioid receptor antagonist naloxone (2 mg/kg, $n = 6$), MOR antagonist CTOP (1.0 mg/kg, $n = 7$), or saline ($n = 6$) on SBI-810 (12 mg/kg)-induced antinociception.

(B) Morphine (10 mg/kg, s.c.) induced CPP and the effects of SBI-810 (12 mg/kg, $n = 8$; 30 mg/kg, $n = 7$) and vehicle ($n = 7$).

(C and D) Acute morphine-induced constipation assessed by GI movement. (C) Photographs of GI charcoal movement after vehicle with morphine (1a and 1b, 10 mg/kg, s.c.), SBI-810 (2a and 2b, 12 mg/kg, i.p.) with morphine. Charcoal was given by oral gavage (5%, 0.1 mL/10 g body weight) 30 min after the drug treatment. (D) GI transit rate. $n = 10$ mice.

(E and F) Chronic opioid-induced withdrawal. (E) Schematic of chronic opioid-induced withdrawal responses 120 min after naloxone injection (2 mg/kg, i.p.). (F) Co-administration of SBI-810 (12 mg/kg, i.p.) with morphine prevented the development of withdrawal responses, as assessed by the cumulative score of 9 individual events, including (1) jumping, (2) teeth chattering, (3) wet-dog shakes, (4) head shakes, (5) grooming, (6) paw tremors, (7) piloerection, (8) salivation, and (9) ejaculation. $n = 7$.

Data are shown as means \pm SEMs. Mice from both sexes were included. Data were statistically analyzed by unpaired t test (D and F), one-way ANOVA (B), and two-way RM-ANOVA (A), followed by Bonferroni post hoc comparisons. * $p < 0.05$, *** $p < 0.001$, **** $p < 0.0001$ for comparisons as indicated. # $p < 0.05$, vs. BL. See also Figure S6 and Table S1 for additional details.

SBI-810 enhanced morphine's antinociception under both acute and chronic conditions (Figures S6A–S6D). Additionally, SBI-810 alleviated morphine-induced hyperalgesia in the von Frey test (Figure S6E). Notably, the effects of SBI-810 were not blocked by the broad opioid receptor antagonist naloxone or the specific MOR antagonist CTOP (Figure 6A), indicating SBI-810's suppression of pain may not require the endogenous opioid system.

We also evaluated SBI-810's abuse potential using the CPP assay. SBI-810 alone did not induce CPP at i.p. doses of 12 and 30 mg/kg (Figure 6B). By contrast, morphine (10 mg/kg subcutaneous [s.c.]) significantly increased CPP vs. the vehicle group ($p < 0.05$), which SBI-810 dose-dependently reduced, with the 30 mg/kg dose significantly reducing morphine-induced CPP to vehicle levels ($p < 0.05$; Figure 6B). Thus, not only is SBI-810 not reinforcing on its own, but it can also negate morphine's addictive effects.

Constipation is a well-recognized side effect of opioid.⁷³ We investigated the impact of SBI-810 on acute morphine-induced constipation by oral gavage with charcoal, followed by examination of gastrointestinal (GI) movement.⁴⁹ We found SBI-810

treatment (12 mg/kg, i.p.) significantly mitigated morphine-induced inhibition of GI transit ($p < 0.001$; Figures 6C and 6D).

A characteristic of opioid addiction is withdrawal behaviors in rodents, including jumping, teeth chattering, wet-dog shakes, head shakes, grooming, paw tremors, piloerection, ejaculation, and salivation, which are indicators of drug dependence.⁷⁴ To examine opioid withdrawal, mice were given escalating doses of morphine twice a day over 5 consecutive days (7.5–50 mg/kg, s.c.), followed by a naloxone challenge after the last morphine injection (Figure 6E). This procedure resulted in the appearance of robust cumulative scores for withdrawal. Remarkably, when the morphine injection was followed with SBI-810 (12 mg/kg, i.p.), the cumulative numbers of withdrawal symptoms were significantly reduced ($p < 0.0001$; Figure 6F). However, in the escalating paradigm where SBI-810 was given 60 min after the final morphine injection and followed by naloxone 60 min later, SBI-810 offered no significant advantage in mitigating the opioid withdrawal response (Figures S6F and S6G). Collectively, our findings indicate that SBI-810 effectively reduces morphine's reinforcing effects and mitigates naloxone-induced withdrawal symptoms in the early phase.

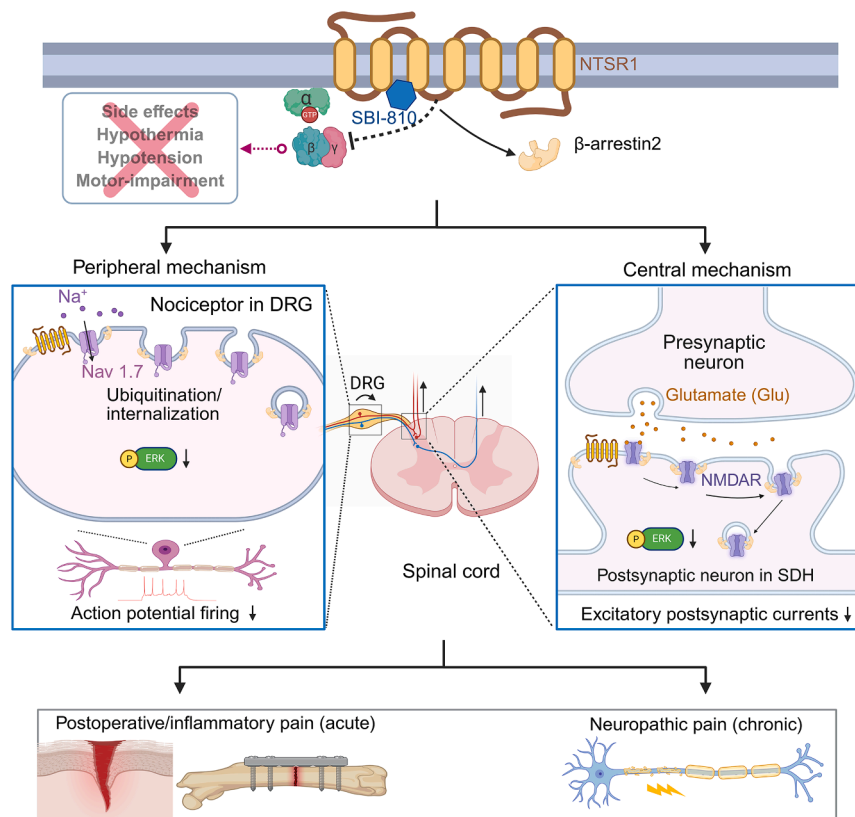


Figure 7. Schematic representation of the central and peripheral mechanisms by which the NTSR1 BAM SBI-810 produces potent analgesia in mouse models of pain through β arr2

SBI-810 not only increases pain thresholds in naive animals but also reduces postoperative pain after incision and bone fracture and inflammatory pain after tissue injury, as well as neuropathic pain after nerve injury. SBI-810 plays a central role in suppressing excitatory synaptic transmission and NMDAR/ERK signaling in spinal cord nociceptive neurons through β arr2. In the periphery, SBI-810 reduces the surface expression of Nav1.7 sodium channels and phosphorylation of ERK and suppresses neuronal excitability of mouse and human nociceptors. It further depresses C-fiber-induced responses *in vivo*. Additionally, SBI-810 inhibits acute opioid-induced CPP and attenuates the constipation and withdrawal responses associated with chronic opioid exposure.

tration, as well as retaining the diminished side effects of NT (e.g., hypotension and hypothermia).^{36,37} While SBI-810 is a β arr2 BAM, there is precedent for β arr2 to play roles in analgesia.³³ Previously, we demonstrated that β arr2 suppresses pain by inhibiting NMDAR signaling in spinal cord neurons.³³ Here, the loss of *Arrb2* led to a transition from acute to

chronic pain. In comparison, spinal cord overexpression of *Arrb2* provided long-lasting pain relief for months in a mouse model of chronic neuropathic pain.³³

In this study, we provided several lines of evidence to demonstrate SBI-810's analgesic actions in various rodent models via NTSR1 and β arr2 (Figure 7). First, systemic and i. t. administration of SBI-810 increased pain thresholds in naive mice under the physiological conditions. Second, the analgesic actions of SBI-810 are lost in *Arrb2*^{-/-} and *Ntsr1*^{-/-} mutant mice, emphasizing the key contributions of the NTSR1- β arr2 axis. Notably, SBI-810 retained full analgesia in *Arrb1*^{-/-} and *Ntsr2*^{-/-} mice, suggesting the analgesic effects are highly selective. Third, SBI-810 provided pain relief across multiple mouse models, including postoperative pain from plantar incisions or bone fractures, inflammatory pain following intraplantar formalin or CFA injections, and neuropathic pain due to SNI or diabetes. Fourth, SBI-810 lacked confounding side effects such as impaired motor function, tactile sensation, or blood perfusion. Lastly, SBI-810 effectively reduced neuropathic pain in the rat model of neuropathic pain after SNI, reinforcing its translational potential.

Mechanistically, we demonstrated SBI-810 attenuates both acute and chronic pain through peripheral and central mechanisms (Figure 7). Crucially, the ERK-signaling pathway in SDH and DRG primary sensory neurons is instrumental in both peripheral sensitization and central sensitization.^{53,55,80} At cellular levels, SBI-810 effectively blocked formalin-induced pERK expression in DRG neurons and NMDA-induced pERK

DISCUSSION

In the present work, we have discovered a role for SBI-810 class drugs in inhibiting acute and chronic pain (Figure 7). As a β arr2-BAM at NTSR1, SBI-810 offers multiple advantages for pain control. As a non-opioid analgesic, SBI-810 not only inhibits pain but also potentiates opioid-induced analgesia, reduces opioid-induced constipation, and reduces chronic opioid-induced antinociceptive tolerance. Moreover, SBI-810 plays a role in mitigating addiction by curbing opioid-induced withdrawal responses. The Helping to End Addiction Long-term (HEAL) Initiative by the National Institutes of Health aims to address two ongoing health crises in the US: unmanaged pain and opioid addiction.¹ The development of SBI-810 as a BAM at NTSR1 aligns well with those objectives.

Recently, BAMs have been proposed as an emerging focus in GPCR drug discovery.^{10,16,40,75,76} Alternative MOR agonists have been developed for pain relief, prompted by the observation that opioid analgesia can be potentiated in *Arrb2* KO mice.³⁰ Structure-based design of opioid analgesics led to the discovery of PZM21, a potent G_i activator with exceptional MOR selectivity and limited recruitment of β arr2.⁷⁷ However, these G-protein-biased agonists may still present opioid-related side effects, including respiratory suppression, analgesic tolerance, and addiction.^{78,79} By comparison, SBI-553 has demonstrated remarkable anti-addiction actions by blocking the motor-enhancing effects of cocaine and amphetamine in the open field and the abusive property of cocaine following self-adminis-

expression in SDH neurons. ERK activation by phosphorylation in nociceptors is well-known to regulate peripheral sensitization via sodium channels such as Nav1.7 and Nav1.8.⁸¹ Consistently, SBI-810 suppressed AP firing in mouse and human DRG neurons *in vitro* and C-fiber activities *in vivo* in a bone fracture model. Dysregulation of Nav1.7 ubiquitination in DRG neurons has been implicated in the pathogenesis of neuropathic pain.⁶⁴ Here, SBI-810 not only increased Nav1.7 ubiquitination but also reduced its surface expression in DRG neurons. In spinal cord slices, SBI-810 suppressed NMDA-induced currents and sEPSCs in SDH neurons and reduced surface expression of GluN2B.

At the behavioral levels, SBI-810 attenuated pain via systemic, i.e., intra-ganglionic, or peri-sciatic routes, indicating its multiple levels of actions as a BAM. In the formalin model, SBI-810 blocked both phase I and phase II nocifensive responses. These findings underscore a crosstalk between NSTR1/ β arr2 in the regulation of peripheral sensitization through the ERK/Nav1.7 pathway or central sensitization through the ERK/NMDAR pathway.

Our findings also emphasized the synergistic antinociceptive effects between NT and SBI-810. Endogenous NT is essential for the analgesic effects of SBI-810, and this effect is compromised by the NTSR1 antagonist. Additionally, while low doses of either NT or SBI-810 alone failed to alter PWT in naive mice, their combination significantly increased PWT. These results suggest that SBI-810 cooperates with endogenous NT to modulate pain. The interaction provides a clear demonstration of how a GPCR allosteric modulator can synergistically interact with its endogenous ligand to amplify biological functions.

Recently, the FDA approved VX-548, a selective Nav1.8 inhibitor, for treating acute postoperative pain.⁶

Presently, VX-548 is also being evaluated for chronic pain in a clinical study focused on painful diabetic neuropathy. However, the outcomes of a phase II placebo-controlled trial for lumbosacral radiculopathy were not promising, as VX-548's effects were comparable to those of the placebo group.⁷ These results suggest that targeting peripheral mechanisms alone may not be sufficient for treating chronic pain. By contrast, the effectiveness of our NTSR1 BAM in both acute and chronic pain models highlights the importance of addressing central mechanisms. Notably, SBI-810 does not exhibit the central side effects of cognitive impairment associated with gabapentin.

Limitations of the study

This study has several limitations. Firstly, while we have demonstrated the synergistic antinociceptive effects of SBI-810 and NT, the precise binding mechanism of SBI-810 to NTSR1 and its influence on receptor conformation, both in the presence and absence of NT, remain obscure. Further structural and binding studies are needed to elucidate SBI-810's impact on downstream G-protein- and β arr-signaling pathways. Additionally, SBI-810 may interact with pain targets other than sodium channels and NMDARs through β arr or G-protein-mediated pathways. While this research clarifies the peripheral and spinal cord mechanisms by which SBI-810 inhibits nociceptive transmission, further studies are necessary to investigate its supraspinal effects on reward and pain circuits in specific brain regions. Moreover, investigating the potential roles of NT and additional

NTSR1 BAMs in other disease contexts such as diabetes, obesity, and cancer could provide valuable insights not only in mechanistic actions but also in therapeutic potentials.

RESOURCE AVAILABILITY

Lead contact

Requests for further information and resources should be directed to and will be fulfilled by the lead contact, Ru-Rong Ji (ru-rong.ji@duke.edu).

Materials availability

This study did not generate new reagents.

Data and code availability

Statistical data are available for download from [Table S1](#).

ACKNOWLEDGMENTS

We thank Dr. Robert Lefkowitz at Duke University for providing *Arrb1/Arreb2* KO mice. TRUPATH was a gift from Bryan Roth. This work was supported by DoD grants W81XWH2210266 to L.S.B. and L.M.S. and W81XWH2210267 to R.-R.J. This work was also supported by NIH grants R01NS131812 and R61NS138215 and DoD grants W81XWH2110756, W81XWH2110885, and W81XWH-22-1-0646 to R.-R.J.; R00DA048970 to L.M.S.; and R01DA061773 to L.M.S. and S.H.O.

AUTHOR CONTRIBUTIONS

Conceptualization, R.-R.J., M.G.C., L.S.B., L.M.S., and W.C.W.; methodology, R.G., O.C., Y.Z., Y.L., S.B., S.C., G.C., R.-G.X., W.H., R.Z., S.S., K.L.P., M.N. M., A.R.A., and I.S.; supervision, R.-R.J., L.S.B., L.M.S., and W.C.W.; validation, Y.L. and W.H.; investigation, I.S., M.R.J., and S.H.O.; writing, R.-R.J., W.C.W., L.S.B., and R.G.; and all authors reviewed the manuscript.

DECLARATION OF INTERESTS

Duke University has filed US Provisional Patent Application 63/689,904, "Methods for treating and/or preventing acute and chronic pain through the use of BAMs of the neurotensin receptor 1" (inventors: R.-R.J., L.S.B., W.C.W., and L.M.S.), and US Patent Application 18/560,394, "Non-opioid analgesics for the treatment of acute and chronic pain methods of using same" (inventors: L.S.B., M.G.C., L.M.S., and R.-R.J.).

STAR★METHODS

Detailed methods are provided in the online version of this paper and include the following:

- [KEY RESOURCES TABLE](#)
- [EXPERIMENTAL MODEL AND STUDY PARTICIPANT DETAILS](#)
 - Animals
 - Human DRG samples
- [METHOD DETAILS](#)
 - Reagents
 - Rodent models of acute and chronic pain and drug treatment
 - Behavioral tests in mice and rats
 - Hemodynamic assay for hind limb blood flow monitoring by laser speckle contrast imaging (LSCI) in mice
 - Gastrointestinal transit assay in mice
 - BRET1 β -arrestin recruitment assay in HEK293T cells
 - BRET2 G protein activation assay in HEK293T cells
 - *NTSR1* mutagenesis and β -arrestin recruitment assay in HEK293 cells
 - Nav1.7 pull down and ubiquitination detection in mouse DRG
 - Western blot in mouse DRG and spinal cords
 - Quantitative real-time RT-PCR in mouse spinal cords
 - Immunohistochemistry (IHC) in mouse DRG and spinal cords

- *In situ* hybridization (ISH) and double staining with IHC in mouse spinal cords
- Proximity ligation assay (PLA) in cultured mouse DRG and spinal cord neurons
- Flow cytometry analysis in mouse DRG and spinal cord
- Preparation of the mouse spinal cord slices and whole-cell patch-clamp recordings
- Whole-cell patch clamp recordings in dissociated mouse DRG neurons
- Primary culture and whole cell patch clamp recordings from human DRG neurons
- Electromyography (EMG) in mice
- Computer simulations and *in silico* modeling
- **QUANTIFICATION AND STATISTICAL ANALYSIS**

SUPPLEMENTAL INFORMATION

Supplemental information can be found online at <https://doi.org/10.1016/j.cell.2025.04.038>.

Received: November 8, 2024

Revised: March 12, 2025

Accepted: April 28, 2025

Published: May 19, 2025

REFERENCES

1. Volkow, N.D., and Collins, F.S. (2017). The Role of Science in Addressing the Opioid Crisis. *N. Engl. J. Med.* 377, 391–394. <https://doi.org/10.1056/NEJMs1706626>.
2. Akopian, A.N., Sivilotti, L., and Wood, J.N. (1996). A tetrodotoxin-resistant voltage-gated sodium channel expressed by sensory neurons. *Nature* 379, 257–262. <https://doi.org/10.1038/379257a0>.
3. Akopian, A.N., Souslova, V., England, S., Okuse, K., Ogata, N., Ure, J., Smith, A., Kerr, B.J., McMahon, S.B., Boyce, S., et al. (1999). The tetrodotoxin-resistant sodium channel SNS has a specialized function in pain pathways. *Nat. Neurosci.* 2, 541–548. <https://doi.org/10.1038/9195>.
4. Cox, J.J., Reimann, F., Nicholas, A.K., Thornton, G., Roberts, E., Springell, K., Karbani, G., Jafri, H., Mannan, J., Raashid, Y., et al. (2006). An SCN9A channelopathy causes congenital inability to experience pain. *Nature* 444, 894–898. <https://doi.org/10.1038/nature05413>.
5. Moreno, A.M., Alemán, F., Catroli, G.F., Hunt, M., Hu, M., Dailamy, A., Pla, A., Woller, S.A., Palmer, N., Parekh, U., et al. (2021). Long-lasting analgesia via targeted *in situ* repression of Na(V)1.7 in mice. *Sci. Transl. Med.* 13, eaay9056. <https://doi.org/10.1126/scitranslmed.aay9056>.
6. Jones, J., Correll, D.J., Lechner, S.M., Jazic, I., Miao, X., Shaw, D., Simard, C., Osteen, J.D., Hare, B., Beaton, A., et al. (2023). Selective Inhibition of Na(V)1.8 with VX-548 for Acute Pain. *N. Engl. J. Med.* 389, 393–405. <https://doi.org/10.1056/NEJMoa2209870>.
7. Alsaloum, M., Dib-Hajj, S.D., Page, D.A., Ruben, P.C., Krainer, A.R., and Waxman, S.G. (2025). Voltage-gated sodium channels in excitable cells as drug targets. *Nat. Rev. Drug Discov.* <https://doi.org/10.1038/s41573-024-01108-x>.
8. Woolf, C.J. (2011). Central sensitization: implications for the diagnosis and treatment of pain. *Pain* 152, S2–S15. <https://doi.org/10.1016/j.pain.2010.09.030>.
9. Ji, R.R., Nackley, A., Huh, Y., Terrando, N., and Maixner, W. (2018). Neuroinflammation and Central Sensitization in Chronic and Widespread Pain. *Anesthesiology* 129, 343–366. <https://doi.org/10.1097/ALN.0000000000002130>.
10. Wooten, D., Christopoulos, A., and Sexton, P.M. (2013). Emerging paradigms in GPCR allostery: implications for drug discovery. *Nat. Rev. Drug Discov.* 12, 630–644. <https://doi.org/10.1038/nrd4052>.
11. Conflitti, P., Lyman, E., Sansom, M.S.P., Hildebrand, P.W., Gutiérrez-de-Terán, H., Carloni, P., Ansell, T.B., Yuan, S., Barth, P., Robinson, A.S., et al. (2025). Functional dynamics of G protein-coupled receptors reveal new routes for drug discovery. *Nat. Rev. Drug Discov.* 24, 251–275. <https://doi.org/10.1038/s41573-024-01083-3>.
12. Corder, G., Castro, D.C., Bruchas, M.R., and Scherrer, G. (2018). Endogenous and Exogenous Opioids in Pain. *Annu. Rev. Neurosci.* 41, 453–473. <https://doi.org/10.1146/annurev-neuro-080317-061522>.
13. Solway, B., Bose, S.C., Corder, G., Donahue, R.R., and Taylor, B.K. (2011). Tonic inhibition of chronic pain by neuropeptide Y. *Proc. Natl. Acad. Sci. USA* 108, 7224–7229. <https://doi.org/10.1073/pnas.1017719108>.
14. Bang, S., Jiang, C., Xu, J., Chandra, S., McGinnis, A., Luo, X., He, Q., Li, Y., Wang, Z., Ao, X., et al. (2024). Satellite glial GPR37L1 and its ligand maresin 1 regulate potassium channel signaling and pain homeostasis. *J. Clin. Invest.* 134, e173537. <https://doi.org/10.1172/JCI173537>.
15. Rangari, V.A., O'Brien, E.S., Powers, A.S., Slivicki, R.A., Bertels, Z., Apourchoux, K., Aydin, D., Ramos-Gonzalez, N., Mwirigi, J., Lin, L., et al. (2025). A cryptic pocket in CB1 drives peripheral and functional selectivity. *Nature* 640, 265–273. <https://doi.org/10.1038/s41586-025-08618-7>.
16. Draper-Joyce, C.J., Bhola, R., Wang, J., Bhattarai, A., Nguyen, A.T.N., Cowie-Kent, I., O'Sullivan, K., Chia, L.Y., Venugopal, H., Valant, C., et al. (2021). Positive allosteric mechanisms of adenosine A(1) receptor-mediated analgesia. *Nature* 597, 571–576. <https://doi.org/10.1038/s41586-021-03897-2>.
17. Feng, Y.P., Wang, J., Dong, Y.L., Wang, Y.Y., and Li, Y.Q. (2015). The roles of neurotensin and its analogues in pain. *Curr. Pharm. Des.* 21, 840–848. <https://doi.org/10.2174/1381612820666141027124915>.
18. Carraway, R., and Leeman, S.E. (1973). The isolation of a new hypotensive peptide, neurotensin, from bovine hypothalamus. *J. Biol. Chem.* 248, 6854–6861. [https://doi.org/10.1016/S0021-9258\(19\)43429-7](https://doi.org/10.1016/S0021-9258(19)43429-7).
19. Uhl, G.R., Bennett, J.P., and Snyder, S.H. (1977). Neurotensin, a Central Nervous-System Peptide – Apparent Receptor-Binding in Brain Membranes. *Brain Res.* 130, 299–313. [https://doi.org/10.1016/0006-8993\(77\)90277-3](https://doi.org/10.1016/0006-8993(77)90277-3).
20. Yaksh, T.L., Michener, S.R., Bailey, J.E., Harty, G.J., Lucas, D.L., Nelson, D.K., Roddy, D.R., and Go, V.L. (1988). Survey of distribution of substance P, vasoactive intestinal polypeptide, cholecystokinin, neurotensin, Met-enkephalin, bombesin and PHI in the spinal cord of cat, dog, sloth and monkey. *Peptides* 9, 357–372. [https://doi.org/10.1016/0196-9781\(88\)90272-0](https://doi.org/10.1016/0196-9781(88)90272-0).
21. Yaksh, T.L., Schmauss, C., Micevych, P.E., Abay, E.O., and Go, V.L. (1982). Pharmacological studies on the application, disposition, and release of neurotensin in the spinal cord. *Ann. N. Y. Acad. Sci.* 400, 228–243. <https://doi.org/10.1111/j.1749-6632.1982.tb31572.x>.
22. Zhang, X., Bao, L., Xu, Z.Q., Diez, M., Frey, P., and Hökfelt, T. (1996). Peripheral axotomy induces increased expression of neurotensin in large neurons in rat lumbar dorsal root ganglia. *Neurosci. Res.* 25, 359–369. [https://doi.org/10.1016/0168-0102\(96\)01062-0](https://doi.org/10.1016/0168-0102(96)01062-0).
23. Smith, K.E., Boules, M., Williams, K., and Richelson, E. (2012). NTS1 and NTS2 mediate analgesia following neurotensin analog treatment in a mouse model for visceral pain. *Behav. Brain Res.* 232, 93–97. <https://doi.org/10.1016/j.bbr.2012.03.044>.
24. Nemeroff, C.B., Osbahr, A.J., 3rd, Manberg, P.J., Ervin, G.N., and Prange, A.J., Jr. (1979). Alterations in nociception and body temperature after intracisternal administration of neurotensin, beta-endorphin, other endogenous peptides, and morphine. *Proc. Natl. Acad. Sci. USA* 76, 5368–5371. <https://doi.org/10.1073/pnas.76.10.5368>.
25. Bredeloux, P., Costentin, J., and Dubuc, I. (2006). Interactions between NTS2 neurotensin and opioid receptors on two nociceptive responses assessed on the hot plate test in mice. *Behav. Brain Res.* 175, 399–407. <https://doi.org/10.1016/j.bbr.2006.09.016>.
26. Fosgerau, K., and Hoffmann, T. (2015). Peptide therapeutics: current status and future directions. *Drug Discov. Today* 20, 122–128. <https://doi.org/10.1016/j.drudis.2014.10.003>.

27. Kitabgi, P. (2002). Targeting neurotensin receptors with agonists and antagonists for therapeutic purposes. *Curr. Opin. Drug Discov. Dev.* 5, 764–776.
28. Shenoy, S.K., and Lefkowitz, R.J. (2011). beta-Arrestin-mediated receptor trafficking and signal transduction. *Trends Pharmacol. Sci.* 32, 521–533. <https://doi.org/10.1016/j.tips.2011.05.002>.
29. Reiter, E., Ahn, S., Shukla, A.K., and Lefkowitz, R.J. (2012). Molecular mechanism of beta-arrestin-biased agonism at seven-transmembrane receptors. *Annu. Rev. Pharmacol. Toxicol.* 52, 179–197. <https://doi.org/10.1146/annurev.pharmtox.010909.105800>.
30. Bohn, L.M., Lefkowitz, R.J., Gainetdinov, R.R., Peppel, K., Caron, M.G., and Lin, F.T. (1999). Enhanced morphine analgesia in mice lacking beta-arrestin 2. *Science* 286, 8141. <https://doi.org/10.1126/science.286.5449.2495>.
31. Chen, W., ten Berge, D., Brown, J., Ahn, S., Hu, L.A., Miller, W.E., Caron, M.G., Barak, L.S., Nusse, R., and Lefkowitz, R.J. (2003). Dishevelled 2 recruits beta-arrestin 2 to mediate Wnt5A-stimulated endocytosis of Frizzled 4. *Science* 301, 1391–1394. <https://doi.org/10.1126/science.1082808>.
32. Chen, W., Kirkbride, K.C., How, T., Nelson, C.D., Mo, J., Frederick, J.P., Wang, X.F., Lefkowitz, R.J., and Blobel, G.C. (2003). Beta-arrestin 2 mediates endocytosis of type III TGF-beta receptor and down-regulation of its signaling. *Science* 301, 1394–1397. <https://doi.org/10.1126/science.1083195>.
33. Chen, G., Xie, R.G., Gao, Y.J., Xu, Z.Z., Zhao, L.X., Bang, S., Berta, T., Park, C.K., Lay, M., Chen, W., et al. (2016). beta-arrestin-2 regulates NMDA receptor function in spinal lamina II neurons and duration of persistent pain. *Nat. Commun.* 7, 12531. <https://doi.org/10.1038/ncomms12531>.
34. Liu, X.J., Gingrich, J.R., Vargas-Caballero, M., Dong, Y.N., Sengar, A., Beggs, S., Wang, S.H., Ding, H.K., Frankland, P.W., and Salter, M.W. (2008). Treatment of inflammatory and neuropathic pain by uncoupling Src from the NMDA receptor complex. *Nat. Med.* 14, 1325–1332. <https://doi.org/10.1038/nm.1883>.
35. Woolf, C.J., and Salter, M.W. (2000). Neuronal plasticity: increasing the gain in pain. *Science* 288, 1765–1769. <https://doi.org/10.1126/science.288.5472.1765>.
36. Duan, J., Liu, H., Zhao, F., Yuan, Q., Ji, Y., Cai, X., He, X., Li, X., Li, J., Wu, K., et al. (2023). GPCR activation and GRK2 assembly by a biased intracellular agonist. *Nature* 620, 676–681. <https://doi.org/10.1038/s41586-023-06395-9>.
37. Slosky, L.M., Bai, Y., Toth, K., Ray, C., Rochelle, L.K., Badea, A., Chandrasekhar, R., Pogorelov, V.M., Abraham, D.M., Atluri, N., et al. (2020). beta-Arrestin-Biased Allosteric Modulator of NTSR1 Selectively Attenuates Addictive Behaviors. *Cell* 181, 1364–1379.e14. <https://doi.org/10.1016/j.cell.2020.04.053>.
38. Gereau, G.B., Zhou, D., Van Voorhies, K., Tyler, R.E., Campbell, J., Murray, J.G., Alvarez-Pamir, A., Wykoff, L.A., Companion, M.A., Jackson, M.R., et al. (2024). beta-arrestin-biased Allosteric Modulator of Neurotensin Receptor 1 Reduces Ethanol Drinking and Responses to Ethanol Administration in Rodents. Preprint at bioRxiv. <https://doi.org/10.1101/2024.04.10.588903>.
39. Pinkerton, A.B., Peddibhotla, S., Yamamoto, F., Slosky, L.M., Bai, Y., Maloney, P., Hershberger, P., Hedrick, M.P., Falter, B., Ardecky, R.J., et al. (2019). Discovery of beta-Arrestin Biased, Orally Bioavailable, and CNS Penetrant Neurotensin Receptor 1 (NTR1) Allosteric Modulators. *J. Med. Chem.* 62, 8357–8363. <https://doi.org/10.1021/acs.jmedchem.9b00340>.
40. Krumm, B.E., DiBerto, J.F., Olsen, R.H.J., Kang, H.J., Slocum, S.T., Zhang, S., Strachan, R.T., Huang, X.P., Slosky, L.M., Pinkerton, A.B., et al. (2023). Neurotensin Receptor Allosterism Revealed in Complex with a Biased Allosteric Modulator. *Biochemistry* 62, 1233–1248. <https://doi.org/10.1021/acs.biochem.3c00029>.
41. Yaksh, T.L., and Rudy, T.A. (1976). Analgesia mediated by a direct spinal action of narcotics. *Science* 192, 1357–1358. <https://doi.org/10.1126/science.1273597>.
42. Donnelly, C.R., Jiang, C., Andriessen, A.S., Wang, K., Wang, Z., Ding, H., Zhao, J., Luo, X., Lee, M.S., Lei, Y.L., et al. (2021). STING controls nociception via type I interferon signalling in sensory neurons. *Nature* 591, 275–280. <https://doi.org/10.1038/s41586-020-03151-1>.
43. Azzam, A.A.H., and Lambert, D.G. (2022). Preclinical discovery and development of oliceridine (Olinvyk(R)) for the treatment of post-operative pain. *Expert Opin. Drug Discov.* 17, 215–223. <https://doi.org/10.1080/17460441.2022.2008903>.
44. Brennan, T.J., Vandermeulen, E.P., and Gebhart, G.F. (1996). Characterization of a rat model of incisional pain. *Pain* 64, 493–502. [https://doi.org/10.1016/0304-3959\(95\)01441-1](https://doi.org/10.1016/0304-3959(95)01441-1).
45. Tuttle, A.H., Molinaro, M.J., Jethwa, J.F., Sotocinal, S.G., Prieto, J.C., Styner, M.A., Mogil, J.S., and Zylka, M.J. (2018). A deep neural network to assess spontaneous pain from mouse facial expressions. *Mol. Pain* 14, 1744806918763658. <https://doi.org/10.1177/1744806918763658>.
46. Langford, D.J., Bailey, A.L., Chanda, M.L., Clarke, S.E., Drummond, T.E., Echols, S., Glick, S., Ingrao, J., Klassen-Ross, T., Lacroix-Fralish, M.L., et al. (2010). Coding of facial expressions of pain in the laboratory mouse. *Nat. Methods* 7, 447–449. <https://doi.org/10.1038/nmeth.1455>.
47. Zhang, L., Terrando, N., Xu, Z.Z., Bang, S., Jordt, S.E., Maixner, W., Serhan, C.N., and Ji, R.R. (2018). Distinct Analgesic Actions of DHA and DHA-Derived Specialized Pro-Resolving Mediators on Post-operative Pain After Bone Fracture in Mice. *Front. Pharmacol.* 9, 412. <https://doi.org/10.3389/fphar.2018.00412>.
48. Decosterd, I., and Woolf, C.J. (2000). Spared nerve injury: an animal model of persistent peripheral neuropathic pain. *Pain* 87, 149–158. [https://doi.org/10.1016/S0304-3959\(00\)00276-1](https://doi.org/10.1016/S0304-3959(00)00276-1).
49. Wang, Z., Jiang, C., He, Q., Matsuda, M., Han, Q., Wang, K., Bang, S., Ding, H., Ko, M.C., and Ji, R.R. (2020). Anti-PD-1 treatment impairs opioid antinociception in rodents and nonhuman primates. *Sci. Transl. Med.* 12, eaaw6471. <https://doi.org/10.1126/scitranslmed.aaw6471>.
50. Finnerup, N.B., Sindrup, S.H., and Jensen, T.S. (2010). The evidence for pharmacological treatment of neuropathic pain. *Pain* 150, 573–581. <https://doi.org/10.1016/j.pain.2010.06.019>.
51. King, T., Vera-Portocarrero, L., Gutierrez, T., Vanderah, T.W., Dussor, G., Lai, J., Fields, H.L., and Porreca, F. (2009). Unmasking the tonic-aversive state in neuropathic pain. *Nat. Neurosci.* 12, 1364–1366. <https://doi.org/10.1038/nn.2407>.
52. Liang, D.Y., Li, W.W., Nwaneshiudu, C., Irvine, K.A., and Clark, J.D. (2019). Pharmacological Characters of Oliceridine, a mu-Opioid Receptor G-Protein-Biased Ligand in Mice. *Anesth. Analg.* 129, 1414–1421. <https://doi.org/10.1213/ANE.0000000000003662>.
53. Ji, R.R., Baba, H., Brenner, G.J., and Woolf, C.J. (1999). Nociceptive-specific activation of ERK in spinal neurons contributes to pain hypersensitivity. *Nat. Neurosci.* 2, 1114–1119. <https://doi.org/10.1038/16040>.
54. Svensson, C.I., Marsala, M., Westerlund, A., Calcutt, N.A., Campana, W. M., Freshwater, J.D., Catalano, R., Feng, Y., Protter, A.A., Scott, B., et al. (2003). Activation of p38 mitogen-activated protein kinase in spinal microglia is a critical link in inflammation-induced spinal pain processing. *J. Neurochem.* 86, 1534–1544. <https://doi.org/10.1046/j.1471-4159.2003.01969.x>.
55. Dai, Y., Iwata, K., Fukuoka, T., Kondo, E., Tokunaga, A., Yamanaka, H., Tachibana, T., Liu, Y., and Noguchi, K. (2002). Phosphorylation of extracellular signal-regulated kinase in primary afferent neurons by noxious stimuli and its involvement in peripheral sensitization. *J. Neurosci.* 22, 7737–7745. <https://doi.org/10.1523/JNEUROSCI.22-17-07737.2002>.
56. Ikeda, H., Heinke, B., Ruscheweyh, R., and Sandkühler, J. (2003). Synaptic plasticity in spinal lamina I projection neurons that mediate hyperalgesia. *Science* 299, 1237–1240. <https://doi.org/10.1126/science.1080659>.
57. Xu, Z.Z., Liu, X.J., Berta, T., Park, C.K., Lü, N., Serhan, C.N., and Ji, R.R. (2013). Neuroprotectin/protectin D1 protects against neuropathic pain in mice after nerve trauma. *Ann. Neurol.* 74, 490–495. <https://doi.org/10.1002/ana.23928>.

58. Gold, M.S., and Gebhart, G.F. (2010). Nociceptor sensitization in pain pathogenesis. *Nat. Med.* 16, 1248–1257. <https://doi.org/10.1038/nm.2235>.
59. Todd, A.J. (2010). Neuronal circuitry for pain processing in the dorsal horn. *Nat. Rev. Neurosci.* 11, 823–836. <https://doi.org/10.1038/nrn2947>.
60. Braz, J., Solorzano, C., Wang, X., and Basbaum, A.I. (2014). Transmitting Pain and Itch Messages: A Contemporary View of the Spinal Cord Circuits that Generate Gate Control. *Neuron* 82, 522–536. <https://doi.org/10.1016/j.neuron.2014.01.018>.
61. Wang, K., Gu, Y., Liao, Y., Bang, S., Donnelly, C.R., Chen, O., Tao, X., Miranda, A.J., Hilton, M.J., and Ji, R.R. (2020). PD-1 blockade inhibits osteoclast formation and murine bone cancer pain. *J. Clin. Invest.* 130, 3603–3620. <https://doi.org/10.1172/JCI133334>.
62. Xu, Z.Q., Zhang, X., Grillner, S., and Hökfelt, T. (1997). Electrophysiological studies on rat dorsal root ganglion neurons after peripheral axotomy: changes in responses to neuropeptides. *Proc. Natl. Acad. Sci. USA* 94, 13262–13266. <https://doi.org/10.1073/pnas.94.24.13262>.
63. Zhang, X., Xu, Z.Q., Bao, L., Dagerlind, A., and Hökfelt, T. (1995). Complementary distribution of receptors for neurotensin and NPY in small neurons in rat lumbar DRGs and regulation of the receptors and peptides after peripheral axotomy. *J. Neurosci.* 15, 2733–2747. <https://doi.org/10.1523/JNEUROSCI.15-04-02733.1995>.
64. Laedermann, C.J., Cachemaille, M., Kirschmann, G., Pertin, M., Gosselin, R.D., Chang, I., Albesa, M., Towne, C., Schneider, B.L., Kellenberger, S., et al. (2013). Dysregulation of voltage-gated sodium channels by ubiquitin ligase NEDD4-2 in neuropathic pain. *J. Clin. Invest.* 123, 3002–3013. <https://doi.org/10.1172/JCI68996>.
65. Cachemaille, M., Laedermann, C.J., Pertin, M., Abriel, H., Gosselin, R.D., and Decosterd, I. (2012). Neuronal expression of the ubiquitin ligase Nedd4-2 in rat dorsal root ganglia: modulation in the spared nerve injury model of neuropathic pain. *Neuroscience* 227, 370–380. <https://doi.org/10.1016/j.neuroscience.2012.09.044>.
66. Andelic, M., Salvi, E., Marcuzzo, S., Marchi, M., Lombardi, R., Cartelli, D., Cazzato, D., Mehmeti, E., Gelemanovic, A., Paolini, M., et al. (2023). Integrative miRNA-mRNA profiling of human epidermis: unique signature of SCN9A painful neuropathy. *Brain* 146, 3049–3062. <https://doi.org/10.1093/brain/awad025>.
67. Shenoy, S.K., Xiao, K., Venkataramanan, V., Snyder, P.M., Freedman, N.J., and Weissman, A.M. (2008). Nedd4 mediates agonist-dependent ubiquitination, lysosomal targeting, and degradation of the beta2-adrenergic receptor. *J. Biol. Chem.* 283, 22166–22176. <https://doi.org/10.1074/jbc.M709668200>.
68. Shenoy, S.K. (2014). Arrestin interaction with E3 ubiquitin ligases and deubiquitinases: functional and therapeutic implications. *Handb. Exp. Pharmacol.* 219, 187–203. https://doi.org/10.1007/978-3-642-41199-1_10.
69. Jensen, D.D., Lieu, T., Halls, M.L., Veldhuis, N.A., Imlach, W.L., Mai, Q.N., Poole, D.P., Quach, T., Aurelio, L., Conner, J., et al. (2017). Neurokinin 1 receptor signaling in endosomes mediates sustained nociception and is a viable therapeutic target for prolonged pain relief. *Sci. Transl. Med.* 9, eaal3447. <https://doi.org/10.1126/scitranslmed.aal3447>.
70. Shiers, S., Klein, R.M., and Price, T.J. (2020). Quantitative differences in neuronal subpopulations between mouse and human dorsal root ganglia demonstrated with RNAscope in situ hybridization. *Pain* 161, 2410–2424. <https://doi.org/10.1097/j.pain.0000000000001973>.
71. Chang, W., Berta, T., Kim, Y.H., Lee, S., Lee, S.Y., and Ji, R.R. (2018). Expression and Role of Voltage-Gated Sodium Channels in Human Dorsal Root Ganglion Neurons with Special Focus on Nav1.7, Species Differences, and Regulation by Paclitaxel. *Neurosci. Bull.* 34, 4–12. <https://doi.org/10.1007/s12264-017-0132-3>.
72. Chen, G., Kim, Y.H., Li, H., Luo, H., Liu, D.L., Zhang, Z.J., Lay, M., Chang, W., Zhang, Y.Q., and Ji, R.R. (2017). PD-L1 inhibits acute and chronic pain by suppressing nociceptive neuron activity via PD-1. *Nat. Neurosci.* 20, 917–926. <https://doi.org/10.1038/nn.4571>.
73. Farmer, A.D., Holt, C.B., Downes, T.J., Ruggeri, E., Del Vecchio, S., and De Giorgio, R. (2018). Pathophysiology, diagnosis, and management of opioid-induced constipation. *Lancet Gastroenterol. Hepatol.* 3, 203–212. [https://doi.org/10.1016/S2468-1253\(18\)30008-6](https://doi.org/10.1016/S2468-1253(18)30008-6).
74. Burma, N.E., Bonin, R.P., Leduc-Pessah, H., Baimel, C., Cairncross, Z.F., Mousseau, M., Shankara, J.V., Stenkowski, P.L., Baimoukhametova, D., Bains, J.S., et al. (2017). Blocking microglial pannexin-1 channels alleviates morphine withdrawal in rodents. *Nat. Med.* 23, 355–360. <https://doi.org/10.1038/nm.4281>.
75. Slosky, L.M., Caron, M.G., and Barak, L.S. (2021). Biased Allosteric Modulators: New Frontiers in GPCR Drug Discovery. *Trends Pharmacol. Sci.* 42, 283–299. <https://doi.org/10.1016/j.tips.2020.12.005>.
76. Zhang, M., Lan, X., Li, X., and Lu, S. (2023). Pharmacologically targeting intracellular allosteric sites of GPCRs for drug discovery. *Drug Discov. Today* 28, 103803. <https://doi.org/10.1016/j.drudis.2023.103803>.
77. Manglik, A., Lin, H., Aryal, D.K., McCorvy, J.D., Dengler, D., Corder, G., Levit, A., Kling, R.C., Bernat, V., Hübner, H., et al. (2016). Structure-based discovery of opioid analgesics with reduced side effects. *Nature* 537, 185–190. <https://doi.org/10.1038/nature19112>.
78. Ding, H., Kiguchi, N., Perrey, D.A., Nguyen, T., Czoty, P.W., Hsu, F.C., Zhang, Y., and Ko, M.C. (2020). Antinociceptive, reinforcing, and pruritic effects of the G-protein signalling-biased mu opioid receptor agonist PZM21 in non-human primates. *Br. J. Anaesth.* 125, 596–604. <https://doi.org/10.1016/j.bja.2020.06.057>.
79. Araldi, D., Ferrari, L.F., and Levine, J.D. (2018). Mu-opioid Receptor (MOR) Biased Agonists Induce Biphasic Dose-dependent Hyperalgesia and Analgesia, and Hyperalgesic Priming in the Rat. *Neuroscience* 394, 60–71. <https://doi.org/10.1016/j.neuroscience.2018.10.015>.
80. Karim, F., Wang, C.C., and Gereau, R.W. (2001). Metabotropic glutamate receptor subtypes 1 and 5 are activators of extracellular signal-regulated kinase signaling required for inflammatory pain in mice. *J. Neurosci.* 21, 3771–3779. <https://doi.org/10.1523/JNEUROSCI.21-11-03771.2001>.
81. Jiang, B.C., Ling, Y.J., Xu, M.L., Gu, J., Wu, X.B., Sha, W.L., Tian, T., Bai, X. H., Li, N., Jiang, C.Y., et al. (2024). Follistatin drives neuropathic pain in mice through IGF1R signaling in nociceptive neurons. *Sci. Transl. Med.* 16, eadi1564. <https://doi.org/10.1126/scitranslmed.adi1564>.
82. Xu, Z.Z., Kim, Y.H., Bang, S.S., Zhang, Y., Berta, T., Wang, F., Oh, S.B., and Ji, R.R. (2015). Inhibition of mechanical allodynia in neuropathic pain by TLR5-mediated A-fiber blockade. *Nat. Med.* 21, 1326–1331. <https://doi.org/10.1038/nm.3978>.
83. Matsuda, M., Oh-Hashi, K., Yokota, I., Sawas, T., and Amaya, F. (2017). Acquired Exchange Protein Directly Activated by Cyclic Adenosine Monophosphate Activity Induced by p38 Mitogen-activated Protein Kinase in Primary Afferent Neurons Contributes to Sustaining Postincisional Nociception. *Anesthesiology* 126, 150–162. <https://doi.org/10.1097/ALN.0000000000001401>.
84. Handool, K.O., Ibrahim, S.M., Kaka, U., Omar, M.A., Abu, J., Yusoff, M.S. M., and Yusof, L.M. (2018). Optimization of a closed rat tibial fracture model. *J. Exp. Orthop.* 5, 13. <https://doi.org/10.1186/s40634-018-0128-6>.
85. Duan, B., Cheng, L., Bourane, S., Britz, O., Padilla, C., Garcia-Campmany, L., Krashes, M., Knowlton, W., Velasquez, T., Ren, X., et al. (2014). Identification of spinal circuits transmitting and gating mechanical pain. *Cell* 159, 1417–1432. <https://doi.org/10.1016/j.cell.2014.11.003>.
86. Zhao, J., Bang, S., Furutani, K., McGinnis, A., Jiang, C., Roberts, A., Donnelly, C.R., He, Q., James, M.L., Berger, M., et al. (2023). PD-L1/PD-1 checkpoint pathway regulates hippocampal neuronal excitability and learning and memory behavior. *Neuron* 111, 2709–2726.e9. <https://doi.org/10.1016/j.neuron.2023.05.022>.
87. Wang, Z.L., Li, N., Wang, P., Tang, H.H., Han, Z.L., Song, J.J., Li, X.H., Yu, H.P., Zhang, T., Zhang, R., et al. (2016). Pharmacological characterization of EN-9, a novel chimeric peptide of endomorphin-2 and neuropeptide FF that produces potent antinociceptive activity and limited tolerance. *Neuropharmacology* 108, 364–372. <https://doi.org/10.1016/j.neuropharm.2016.03.017>.

88. Olsen, R.H.J., DiBerto, J.F., English, J.G., Glaudin, A.M., Krumm, B.E., Slocum, S.T., Che, T., Gavin, A.C., McCorvy, J.D., Roth, B.L., et al. (2020). TRUPATH, an open-source biosensor platform for interrogating the GPCR transducerome. *Nat. Chem. Biol.* *16*, 841–849. <https://doi.org/10.1038/s41589-020-0535-8>.
89. Wang, Z., Jiang, C., Yao, H., Chen, O., Rahman, S., Gu, Y., Zhao, J., Huh, Y., and Ji, R.R. (2021). Central opioid receptors mediate morphine-induced itch and chronic itch via disinhibition. *Brain* *144*, 665–681. <https://doi.org/10.1093/brain/awaa430>.
90. Park, C.K., Lü, N., Xu, Z.Z., Liu, T., Serhan, C.N., and Ji, R.R. (2011). Resolving TRPV1- and TNF- α -mediated spinal cord synaptic plasticity and inflammatory pain with neuroprotectin D1. *J. Neurosci.* *31*, 15072–15085. <https://doi.org/10.1523/JNEUROSCI.2443-11.2011>.
91. UniProt Consortium (2021). UniProt: the universal protein knowledgebase in 2021. *Nucleic Acids Res.* *49*, D480–D489. <https://doi.org/10.1093/nar/gkaa1100>.
92. Morris, G.M., Huey, R., Lindstrom, W., Sanner, M.F., Belew, R.K., Goodsell, D.S., and Olson, A.J. (2009). AutoDock4 and AutoDockTools4: Automated docking with selective receptor flexibility. *J. Comput. Chem.* *30*, 2785–2791. <https://doi.org/10.1002/jcc.21256>.
93. Pettersen, E.F., Goddard, T.D., Huang, C.C., Couch, G.S., Greenblatt, D.M., Meng, E.C., and Ferrin, T.E. (2004). UCSF Chimera—a visualization system for exploratory research and analysis. *J. Comput. Chem.* *25*, 1605–1612. <https://doi.org/10.1002/jcc.20084>.
94. Jiménez, J., Škalič, M., Martínez-Rosell, G., and De Fabritiis, G. (2018). KDEEP: Protein-Ligand Absolute Binding Affinity Prediction via 3D-Convolutional Neural Networks. *J. Chem. Inf. Model.* *58*, 287–296. <https://doi.org/10.1021/acs.jcim.7b00650>.
95. Bowers, K.J., Chow, D.E., Xu, H., Dror, R.O., Eastwood, M.P., Gregersen, B.A., Klepeis, J.L., Kolossvary, I., Moraes, M.A., Sacerdoti, F.D., et al. (2006). Scalable algorithms for molecular dynamics simulations on commodity clusters43. In *Proceedings of the 2006 ACM/IEEE Conference on Supercomputing (IEEE)*, p. 43. <https://doi.org/10.1109/SC.2006.54>.

STAR★METHODS

KEY RESOURCES TABLE

REAGENT or RESOURCE	SOURCE	IDENTIFIER
Antibodies		
GluN2B/NR2B	NeuroMab	Cat# 75-097; RRID: AB_10673405
GluNA1	Cell Signaling Technology	Cat# 13185; RRID: AB_2732897
GluNA2	Cell Signaling Technology	Cat# 13607; RRID: AB_2650557
Nav1.7 (SCN9A) (extracellular)	Alomone Labs	Cat# ASC-027; RRID: AB_2341069
Nav1.7 (SCN9A)	Alomone Labs	Cat# ASC-008; RRID: AB_2040198
pERK	Cell Signaling Technology	Cat# 9101; RRID: AB_331646
NeuN	Sigma	Cat# ABN90P; RRID: AB_2341095
HA-Tag (C29F4)	Cell Signaling Technology	Cat# 3724; RRID: AB_1549585
HA-Tag (6E2)	Cell Signaling Technology	Cat# 2367; RRID: AB_10691311
Ubiquitin	Santa Cruz	Cat# sc-8017; RRID: AB_628423
GAPDH	Proteintech	Cat# 60004-1-Ig; RRID: AB_2107436
Donkey Rabbit IgG(H+L) CF488A	Biotium	Cat# 20015-1; RRID: AB_10854232
FITC AffiniPure™ Goat Anti-Guinea Pig IgG (H+L)	Jackson ImmunoResearch Labs	Cat# 106-095-003; RRID: AB_2337415
Alexa Fluor® 647 AffiniPure™ Goat Anti-Guinea Pig IgG (H+L)	Jackson ImmunoResearch Labs	Cat# 106-605-003; RRID: AB_2337446
Mouse anti-rabbit IgG-HRP	Santa Cruz	Cat# sc-2357; RRID: AB_628497
IgG Fc	Santa Cruz	Cat# sc-525409; RRID: AB_3101828
IgG-APC	Miltenyi Biotec	Cat# 130-113-758; RRID: AB_2733439
GLAST-PE	Miltenyi Biotec	Cat# 130-118-483; RRID: AB_2733722
CD45-FITC	Thermo Fisher Scientific	Cat# 11-0451-82; RRID: AB_465050
Normal Rabbit IgG	Santa Cruz	Cat# sc-2027; RRID: AB_737197
Anti-Mouse CD16/CD32	BD Pharmingen	Cat# 553141 RRID: AB_394656
Human Nav1.7	Dr. Seok-Yong Lee at Duke University	N/A
Bacterial and virus strains		
pAAV-CamKII-GFP-Cre	Addgene	RRID: Addgene_105551
pAAV-CaMKIIa-mCherry	Addgene	RRID: Addgene_114469
Biological samples		
Human Dorsal Root Ganglion	National Disease Research interchange (NDRI); See STAR Methods for sex and age information	N/A
Chemicals, peptides, and recombinant proteins		
SBI-810	Volochem and Sanford Burnham Prebys Medical Discovery Institute	SBI-0653810
SR 48692	Tocris	Cat# 3721
SR142948A	Millipore/Sigma	Cat# SML0015
CTOP	Abcam	Cat# ab120417
TCN201	Tocris	Cat# 4154
RO25-6981	Tocris	Cat# 1594
NMDA	Tocris	Cat# 0114
Complete Freund's adjuvant (CFA)	Millipore/Sigma	Cat# F5881
Gabapentin	Millipore/Sigma	Cat# G154
Naloxone	Millipore/Sigma	Cat# 1453005

(Continued on next page)

Continued

REAGENT or RESOURCE	SOURCE	IDENTIFIER
Streptozotocin (STZ)	Millipore/Sigma	Cat# 1883-66-4
MG132	Millipore/Sigma	Cat# 474790
Epoxomicin	MCE	Cat# HY-13821
Dyngo-4a (DY-4)	Cayman	Cat# 29479
Pitstop2 (PS-2)	Cayman	Cat# 23885
Activated charcoal	Millipore/Sigma	Cat# C9157
Morphine	Hikma	NDC# 0641-6127-01
Neurotensin (NT) (for <i>in vivo</i>)	MCE	Cat# HY-P0234
Neurotensin (NT) (for <i>in vitro</i>)	Millipore/Sigma	Cat# N6383
Oliceridine (TRV130)	Abmole Bioscience Inc	Cat# M4808
U0126	Calbiochem	Cat# 662005
Lightning-Link® APC Antibody Labeling Kit	Novus	Cat# 705-0010
Protein G-conjugated magnetic beads	Promega	Cat# G7417
Coelenterazine h Cayman	Cayman Chemical	Cat# 16894
Protease inhibitor cocktail	Millipore/Sigma	Cat# P8340
Reverse Transcription System	Promega	Cat# A3500
Coelenterazine 400a (hydrochloride)	Cayman Chemical	Cat# 25738

Critical commercial assays

Genotyping for <i>Ntr1</i> ^{-/-} , <i>Ntr2</i> ^{-/-} and HA- <i>hNTSR1</i> -floxed Strains	Duke University and TransnetYX	N/A
--	--------------------------------	-----

Experimental models: Cell lines

HEK293T/17	American Type Culture Collection (ATCC)	Cat# CRL-11268; RRID: CVCL_1926
------------	---	---------------------------------

Experimental models: Organisms/strains

Mouse: C57BL/6J (Wildtype)	The Jackson Laboratory	RRID: IMSR_JAX:000664
Mouse: CD-1 IGS	Charles River	RRID: IMSR_CRL:022
Rat: Sprague Dawley (CD® IGS)	Charles River	RRID: RGD_1566457
Mouse: <i>Ntr1</i> ^{-/-}	Dr. Marc Caron at Duke University	RRID: IMSR_JAX:005826
Mouse: <i>Ntr2</i> ^{-/-}	Dr. Marc Caron at Duke University	N/A
Mouse: <i>Arb1</i> ^{-/-}	Dr. Robert J. Lefkowitz at Duke University	N/A
Mouse: <i>Arb2</i> ^{-/-}	Dr. Marc Caron at Duke University	N/A
Mouse: HA- <i>hNTSR1</i> -floxed (HA-NTSR1)	Dr. Marc Caron at Duke University	N/A
Mouse: <i>Arb2</i> ^{flox/flox}	Dr. Marc Caron at Duke University	N/A

Oligonucleotides

<i>Arb2</i> primers	Eton Bioscience	Forward: CCAGGTCTTCACGGCCATAG, Reverse: AGTCGAGCCCTAACTGCAAG
<i>Actin</i> primers	Eton Bioscience	Forward: GGCTGTATTCCCCTCCATCG, Reverse: CCAGTTGGTAATGCCATGT

Recombinant DNA

pTwist CMV-human NTSR1 WT-SmBit	Twist Bioscience	synthesis
pTwist CMV-human NTSR1 R166A-SmBit	Twist Bioscience	synthesis
pcDNA3.1-V5-Arrestin2	Addgene	Cat# 201493; RRID: Addgene_201493
pcDNA3.1-Arrestin2-V5	Addgene	Cat# 201494; RRID: Addgene_201494
pcDNA3.1-NabV5-LgBit	Addgene	Cat# 201476; RRID: Addgene_201476
pcDNA3.1-3xHA-NTSR1 (human)-Rluc8	Slosky Lab	PMID: 39605353
pcDNA3.1-3xHA-NTSR1 (mouse)-Rluc8	Slosky Lab	PMID: 39605353
pcDNA3.1-Beta-arrestin2 (human)-mVenus	Slosky Lab	PMID: 39605353
pcDNA3.1-3xHA-NTSR1	cdna.org	#NTSR10TN00

(Continued on next page)

Continued

REAGENT or RESOURCE	SOURCE	IDENTIFIER
pcDNA5/FRT/TO-GAlphaQ-RLuc8	Addgene	Kit #1000000163
pcDNA3.1-Beta3	Addgene	Kit #1000000163
pcDNA3.1-GGamma9-GFP2	Addgene	Kit #1000000163

Software and algorithms

Graphpad Prism 10	GraphPad Software	https://www.graphpad.com
ImageJ	National Institute of Health	https://imagej.net/ij/download.html
Zen system	Zeiss	https://www.zeiss.com/microscopy/us/home.html
BioRender	BioRender, Canada	https://www.biorender.com
ANY-maze	Stoelting Co.	https://www.anymaze.co.uk/index.htm
Clampfit	Molecular Devices	https://www.moleculardevices.com/products/axon-patch-clamp-system/acquisition-andanalysis-software/pclamp-software-suite#gref
pClamp	Molecular Devices	https://www.moleculardevices.com
FACSDiva software v8	BD Bioscience	https://www.bdbiosciences.com/en-us/instruments/research-instruments/research-software/flow-cytometryacquisition/facsdiva-software
PainFace	UNC	https://painface.net
RFLSI analysis	RWD life science	https://www.rwdstco.com/product-item/rfsi-zw-laser-speckle-contrast-imaging-system/
Cytobank	Beckman Coulter Life Sciences	https://www.cytobank.org/cytobank
AutoDock 4	Scripps	https://autodock.scripps.edu/
UCSF Chimera	UCSF	https://www.cgl.ucsf.edu/chimera/
KDEEP	Acellera Therapeutics Inc	https://open.playmolecule.org/
DESMOND 2018-4	D. E. Shaw Research	https://www.deshawresearch.com/resources.html
HawkDock Server V2	Tingjun Hou's Group	http://cadd.zju.edu.cn/hawkdock/
ChemDraw 23.0.1	Revvity Signals Software, Inc	https://revvitysignals.com/products/research/chemdraw

Other

RNAscope probe mouse <i>Ntsr1</i>	Advanced Cell Diagnostics	Cat# 422411
RNAscope probe mouse <i>Ntsr2</i>	Advanced Cell Diagnostics	Cat# 452311
RNAscope Multiplex Fluorescent Reagent Kit v2	Advanced Cell Diagnostics	Cat# 323100
Duolink In Situ Detection Reagents Red	Millipore/Sigma	Cat# DUO92008
Duolink In Situ PLA Probe Anti-Mouse MINUS	Millipore/Sigma	Cat# DUO92004
Duolink In Situ PLA Probe Anti-Rabbit PLUS	Millipore/Sigma	Cat# DUO92002

EXPERIMENTAL MODEL AND STUDY PARTICIPANT DETAILS

Animals

Male and female C57BL/6J mice (8–12 weeks; Jackson Laboratories, Bar Harbor, ME) were used in many behavioral studies. The global *Arrb1*^{-/-} mice were from Dr. Robert J. Lefkowitz at Duke University, and *Ntsr1*^{-/-} the *Arrb2*^{-/-}, and *Arrb2*^{flox/flox} mice were obtained from Drs. Lawrence Barak and Marc Caron at Duke University. *Ntsr2*^{-/-} and *Ntsr1*-HA mice were generated by Dr. Lawrence Barak in the Duke Transgenic Mouse Core Facility. All mouse strains were on a C57BL/6J genetic background and were maintained in the Duke University animal facilities on a 12 h light/dark cycle with access to food and water *ad libitum*. Primer sequences

used for genotyping were included in [Table S2](#). Wild-type (WT) littermates from the genetic lines were used as controls. All of the mutant mice were viable and showed no developmental defects. Young mice (5–7 weeks) were used for electrophysiological studies with spinal cord neurons. Additionally, adult CD1 mice of both sexes (8–12 weeks) Charles River Laboratories, Raleigh, NC) were used for the experiments involving the diabetes model. Sprague Dawley rats (8–12 weeks of both sexes) were obtained from Charles River Laboratories and used in behavioral studies. Animals were randomly assigned to each experimental group. All the animal procedures were approved by the Institutional Animal Care and Use Committee at Duke University.

Human DRG samples

Non-diseased human DRG were obtained from five human donors [(1) Caucasian female-63 years old; (2) Caucasian female-61 years old; (3) Caucasian male-56 years old; (4) Caucasian male-53 years old, and (5) Caucasian female-64 years old)] through NDRI with permission of exemption from the Duke IRB, as previously reported.^{49,82}

METHOD DETAILS

Reagents

SBI-810 was provided by Sanford Burnham Prebys Medical Discovery Institute (La Jolla, CA) and Volochem (West Sacramento, California, 95605). SBI-810 was freshly prepared from powdered stocks and dissolved sequentially by adding DMSO, PEG300, Tween-80, and saline. See more reagents in [Star Methods](#).

Rodent models of acute and chronic pain and drug treatment

We used six mouse models of pain in our studies. (1) The spared nerve injury (SNI) model was conducted to induce long-lasting neuropathic pain.⁴⁸ Mice were anesthetized with isoflurane, and the three branches of the sciatic nerve, the common peroneal nerve, the tibial nerve, and the sural nerve were exposed. The common peroneal and tibial nerves were ligated and cut, leaving the sural nerve intact. (2) The incisional postoperative pain was induced by plantar incision in a hind-paw. A longitudinal 0.5 cm incision was made through the skin, fascia, and plantaris muscle on the plantar aspect using a #15 surgical blade.^{44,83} (3) The tibial bone fracture was performed as previously reported.⁸⁴ An incision was made on the left hindlimb and a stainless steel pin (0.38-mm) was inserted into the intramedullary canal, followed by osteotomy. The incision was closed with 6-0 Prolene sutures. (4) The formalin model was evoked by intraplantar injection of 20 μ l of 5% formalin into a hind paw to induce Phase 1 and Phase 2 spontaneous pain. (5) Complete Freund's adjuvant (CFA, 20 μ l; MilliporeSigma) was injected into the plantar surface of a hind paw to induce persistent inflammatory pain. (6) Streptozotocin (STZ; 150 mg/kg, i.p.) was given to induce diabetic neuropathic pain with elevated blood glucose levels (>400 mg/L). In addition, we established a rat model of SNI using the same surgical procedure applied in mice.

Drug delivery via intraperitoneal and intrathecal route and spinal and DRG microinjection

For intraperitoneal injection, drug and vehicle (100 μ l for mice) was delivered using a Hamilton microsyringe with a 30-gauge needle. For intrathecal injection, animals were anesthetized with isoflurane, and then drug or vehicle (10 μ l for mice and 20 μ l for rats) was delivered using a Hamilton microsyringe with a 30-gauge needle by making a lumbar puncture between the L5 and L6 levels in the spinal cord. For selective deletion of *Arrb2* in excitatory neurons in the spinal cord, *Arrb2*^{fl^{ox}/fl^{ox}} mice were micro-injected in the ipsilateral spinal cord dorsal horn with pENN.AAV.CamKII.HI.GFP-Cre.WPRE.SV40 virus (105551-AAV9; Addgene). The pAAV-CaMKIIa-mCherry control virus (114469-AAV9; addgene) was injected as a control. Intraspinal injections followed established protocols.³³ *Arrb2*^{fl^{ox}/fl^{ox}} mice were anesthetized with isoflurane and the animal's spine was fixed in a stereotaxic apparatus (David Kopf Instruments). After removal of paraspinal muscles on the left side, between the T13 and L1 vertebrae to facilitate access, a partial laminectomy was conducted to create a small window. This window permitted the direct insertion of a glass micropipette (tip diameter: 10–20 μ m) into the spinal cord dorsal horn, in a location approximately 500 μ m lateral from the midline. The micropipette was connected with tubing to a Hamilton syringe in an UltraMicroPump injection system (World Precision Instruments). At a depth 150 μ m from the surface of the dorsal root entry zone, a single injection of AAV9 virus solution (0.6 μ L, 1×10^{13} vg/mL) was delivered into the spinal dorsal horn at a rate of 60 nL/min. The pipette was removed 5 min after injection. For DRG microinjection, the process was performed as described above for the spinal microinjection. In brief, a midline incision was made in the lower lumbar-back region and the L4/L5 DRG were exposed by partial laminectomy. The vehicle or SBI-810 (1 μ l) was microinjected into the DRG by a glass micropipette at a rate of 10 nL/min.

Behavioral tests in mice and rats

All animals were habituated to the testing environment for at least 2 days prior to testing. All behavioral testing was conducted blindly.

von Frey test in mice

Mechanical sensitivity was assessed with von Frey hairs by logarithmically increasing stiffness (0.02–2.56; Stoelting), presented perpendicularly to the central plantar surface and expressed as paw withdrawal threshold (PWT).

Paw Randall-Selitto test in rats

The Randall-Selitto paw-pressure test was conducted using an analgesiometer (Ugo Basile, Italy) to evaluate mechanical nociception in rats. During the test, the operator applied a constantly increasing pressure to the dorsal surface of the hind paw using a blunt conical probe by depressing a pedal switch and released the pedal when the rat displayed a pain response. The nociceptive

threshold was defined as the force (in grams) at which the rat withdrew its paw or exhibited a clear sign of discomfort or escape. Mechanical sensitivity was measured by recording two readings at 5-minute intervals, with the mean value used as the mechanical nociceptive threshold. To ensure animal safety and prevent tissue damage, a cutoff threshold of 300 g was applied.

Cotton-swab and sticky-tape tests for tactile sensitivity assessment in mice

Animals were habituated in a plexiglass chamber placed on a metal mesh floor for 30 min before testing. For cotton swab test, a cotton swab was fluffed to three times its original size. The hind paw was brushed from heel to toe with the swab 10 times, with 1-minute intervals between each brushing. Reactions such as paw flicking or withdrawal were recorded. For sticky tape test, a strip of tape (3 cm × 1 cm) was placed on the dorsum of the hind paw. Animals' attempts to remove the tape (shaking, scratching, or biting) were observed over a 5-min period.⁸⁵

Hargreaves, tail-flick, and hot plate tests for heat pain in mice

Heat pain was assessed using a Hargreaves radiant heat apparatus (IITC Life Science) and expressed as paw-withdrawal latency. The basal paw withdrawal latency was adjusted to 9–12 s, with a cutoff of 20 s to avoid tissue damage. For the tail-flick test, mice were gently held by hand with a terry glove with the tail exposed. The distal 3 cm tip of the tail was immersed into a 50°C hot water bath. The latency to tail-flick was measured as the time the mouse flicked or removed its tail from the water, with a maximum cut-off value of 15 s to prevent thermal injury. The tail-flick latency was determined both before and after drug administration. The data were expressed as the maximum possible effect (MPE) where $MPE (\%) = 100 \times [(post\text{-}drug\ response - baseline\ response) / (cutoff\ response - baseline\ response)]$. For the hot-plate test, mice were placed on the hot plate set to 53°C, and the time for the mouse to flick its paw, lick its paw, or jump was scored. A maximum cut-off value of 40 s was set to avoid thermal injury.

Dry ice and acetone tests for cold pain in mice

Cold pain was assessed in the dry ice and acetone tests. In the acute dry ice test, a syringe was filled with dry ice and was placed next to the glass beneath the paw. Hind-paw withdrawal latencies were recorded for 2–3 trials per paw at each time-point, with a third trial omitted if the differences between the first two trials was ≤ 3 s. In the chronic cold-pain condition, Acetone (20 μ L/application) was gently administered by syringe to the underside of a hind-paw through a mesh floor. Responses to acetone were measured by calculating the duration (s) of paw lifting, licking, flinching, or flicking.

Open field and rotarod tests in mice

To assess locomotor function, mice underwent open field and rotarod testing. In the open field test, each mouse was placed in the center of a 45 × 45 cm square arena (TAP Plastics) for a 10-min session, where locomotor activity was recorded by an overhead webcam connected to a laptop. ANY-maze software (Stoelting Co.) was used to automatically track and analyze the animals' movements, including the total distance traveled during the session. In the rotarod test, which evaluates both motor coordination and potential locomotor impairment, mice were first acclimated to the behavioral testing room for 30 min. Testing was conducted using a rotarod system (IITC Life Science), where each mouse completed three trials, with 10-min rest intervals between trials. During each trial, the rotation speed gradually increased from 4 to 28 r.p.m. over a 3-min period. The latency to fall was recorded for each trial and then averaged to assess overall performance.

Conditioned place preference (CPP) test in mice

All mice were subjected to 4 days of preconditioning habituation for 30 min under low-light conditions between 08:00–16:00 h using a two-compartment CPP chamber (Med Associates), where the compartments differed in visual and tactile cues. On the last preconditioning day, motor activities of the mice were tracked over 15 min with ANY-Maze software (Stoelting). Mice demonstrating a strong preference for one chamber over the other (>80% preference) were excluded from the study. During conditioning days (day 5–7), two daily pairing sessions were conducted that were separated by 4 h, with the vehicle pairing occurring in the morning and the morphine or/and SBI-810 pairing in the afternoon session. Twenty-four h after completing the last pairing (i.e., day 7), mice were placed into the CPP apparatus with access to both chambers, their behavior was recorded for 15 min, and their responses were analyzed using ANY-Maze software to determine their chamber preferences. The CPP score was calculated according to the following formula for time spent in the baseline preferred chamber: post-preference (s) minus pre-preference time (s).

Novel object recognition (NOR) test for cognitive behavior in mice

On day 1, mice were placed in a 30 × 30 × 30 cm square arena (TAP plastics) for habituation. On day 2, two identical objects were positioned in opposite corners of the arena. After a 5-min exploration, mice were returned to their home cages for a 0.5-h retention interval. Following this interval, one of the identical objects was replaced with a new object for the novel object recognition test. After the retention interval, mice were placed back into the arena for 5 min of exploration. Valid exploration was defined as the mouse touching an object with its nose or focusing on the object within < 1 cm. Actions such as turning away, climbing, or sitting on the object were considered invalid. A discrimination index (DI) was used to evaluate exploration time between the familiar and novel objects, calculated as: $DI = (TN - TF) / (TN + TF) \times 100\%$, where TN is the time spent exploring the novel object and TF was the time spent exploring the familiar object. Animal behaviors were video-recorded and analyzed by an experimenter blinded to the testing conditions. Data were excluded if the total exploration time is less than 10 sec.⁸⁶

Mouse grimace scale

Mice were placed individually into a custom-built chamber as part of a four-cubicle array, each measuring 5 × 12 × 6 cm, with three stainless steel walls and a transparent acrylic ceiling. A digital video camera was positioned 0.25 m from the open-side and was used to film the facial responses of the mice in the cubicle array. After a habituation period for 30 min, mice were filmed for a 5-min baseline session before incision surgery. Subsequently, mice were filmed at 3, 6, and 24 h post-surgery at 5 min intervals. Individual frames

from the video-recordings were scored by a blinded observer every 10 s where values of 0, 1, or 2 (0: no response, 1: moderate response, 2: full response) were used for each of the five mouse grimace scale (MGS) action units.⁴⁵ These units included: orbital tightening, nose bulge, cheek bulge, ear position, and whisker change. The final MGS score was the summed score across the five action units, ranging from 0 to 10.

Morphine withdrawal responses in mice

Mice were subjected to daily morphine treatment (s.c.) with escalating doses (7.5 and 15 mg/kg on day 1, 20 and 25 mg/kg on day 2, 30 and 35 mg/kg on day 3, 40 and 45 mg/kg on day 4, and 50 mg/kg on day 5). On day 5 after the last dose of morphine, animals received naloxone (2 mg/kg, i.p.) 120 min later to stimulate withdrawal responses. A cumulative withdrawal score was calculated based on the following behaviors: jumping, teeth chattering, wet-dog shakes, head-shakes, grooming, paw tremors, piloerection, salivation, and ejaculation.⁷⁴

Opioid-induced tolerance and opioid-induced hyperalgesia in mice

To produce morphine's antinociceptive tolerance model, mice received daily subcutaneous injections of morphine (10 mg/kg, s.c.) for six consecutive days. Hot-plate latencies were measured before and 1 h after each morphine injection. % MPE values were used to compare antinociceptive effects and assess tolerance development. For producing opioid-induced hyperalgesia (OIH) model, mice received twice-daily subcutaneous injections of morphine (10 mg/kg, s.c.) for six consecutive days. Morphine-induced hyperalgesia was assessed using the von Frey test from Day 7 to Day 9 after the first injection.

Hemodynamic assay for hind limb blood flow monitoring by laser speckle contrast imaging (LSCI) in mice

One day before the test, mice were shaved on the left hind limb. After a brief anesthesia with isoflurane, mice were placed in the prone position on a thermostatic mouse plate for blood flow monitoring of the left hind limb using the LSCI system from RWD. The operators were blinded to the group allocation. The LSCI system was focused on the mouse limb to obtain a clear color map. Blood flow was monitored at baseline and then 15 min and 1 h after intrathecal injection of neurotensin (22 nmol) or SBI-810 (22 nmol). Continuous monitoring was performed for 60 seconds. The region of interest (ROI) was set to measure the ROI value representing the blood flow in the selected area. The images and data were analyzed using RFLSI analysis software (RWD Life Science).

Gastrointestinal transit assay in mice

Morphine induced constipation was evaluated by gastrointestinal transit (GIT) test as previously reported.^{61,87} Mice were fasted for 16 h with water available *ad libitum* before experiment. Mice were administered with saline or morphine (10 mg/kg, s.c.) 30 min before oral administration of charcoal meal (0.1 ml/10 g body weight, in an aqueous suspension of 5% charcoal and 10% gum arable, Sigma). Animals were sacrificed 30 min after charcoal meal administration, and we measured the length of the small intestine and the distance by which the charcoal traveled and presented data as GIT%.

BRET1 β -arrestin recruitment assay in HEK293T cells

Recruitment of Venus-tagged human or mouse β -arrestin2 to Renilla luciferase (Rluc8)-tagged human NTSR1 was assessed in HEK293T cells using a bioluminescence resonance energy transfer 1 (BRET) assay, as described.³⁷ On day 1, HEK293T cells were plated in 6-well plates (750,000/well) in growth media. On day 2, cells were transiently transfected with Rluc8-tagged NTSR1 (100 ng/well) or Venus-tagged β -arrestin2 (1.4 μ g/well) using calcium phosphate. On day 3, cells were plated onto poly-D-lysine-coated [100 ng/mL], clear bottom, white-walled 96-well plates (40,000 cells/well) in Opti-MEM containing 2% FBS and 1x antibiotic antimycotic solution. On day 4, cells were incubated in 80 μ l/well Hanks' Balanced Salt solution (HBSS) containing calcium and magnesium and 20 mM HEPES for 5-6 hr prior to treatment. Treatments were freshly prepared in HBSS with 5% 2-hydroxypropyl- β -cyclodextrin from 50 mM DMSO (SBI-810, SR142948A) or 2 mM 80% glycerol (NT) stocks. A white vinyl sticker was placed on the bottom of the plate. 10 μ l/well of 10x SBI-810, or NT added 10 min prior to reading. 10 μ l/well of a 10x concentration of coelenterazine h (final concentration 4.7 μ M; Cayman Chemical Co., Ann Arbor, MI, USA) was added 5 min prior to reading. For SBI-810 and NT combination studies, cells were incubated in 70 μ l/well HBSS and pre-treated with 10 μ l 10x SBI-810 pretreatments 10 min prior to NT application. After treatment with coelenterazine h, plates were protected from light. Plates were read at 475-30 nm and 535-30 nm on a CLARIOstar Plus microplate reader (BMG Labtech, Ortenberg, Germany) set at 35°C 5, 10, 15, and 30 min post-treatment. BRET1 ratios were computed as the ratio of Venus (535 nm) to RLuc8 (475 nm) emission. The Δ net BRET ratio was calculated by subtracting the stimulated Venus/Rluc8 ratios from control Venus/Rluc8 ratios for each read. The maximum Δ net BRET ratio over time was averaged within treatments and combined between experiments. Data are presented as mean Δ net BRET ratio \pm SEM from at least three independent experiments.

BRET2 G protein activation assay in HEK293T cells

Activation of Gq by NTSR1 was assessed using the TRUPATH BRET2 assay platform.⁸⁸ On day 1, HEK293T cells were plated in 6-well plates (750,000/well) in DMEM containing 10% FBS and 1% 1x antibiotic antimycotic solution. On day 2, cells were transiently transfected with 3xHA-NTSR1 (200 ng/well), G α q-Rluc8, G β 3 (100 ng/well), and GFP2-tagged G γ 9 (100 ng/well) using calcium phosphate. On day 3, cells were plated (25,000 cells/well) onto poly-D-lysine-coated [100 ng/mL], clear bottom, white-walled 96-well plates in Opti-MEM containing 2% FBS and 1% 1x antibiotic antimycotic solution. On day 4, cells were incubated in 70 or 80 μ l/well HBSS containing calcium and magnesium and 20 mM HEPES for 5-6 hr prior to treatment. Treatments were freshly prepared

in HBSS with 5% 2-hydroxypropyl- β -cyclodextrin from 50 mM DMSO (SBI-810, SR142948A) or 2 mM 80% glycerol (NT) stocks. All plates were allowed to cool for 10 min until they reached approximately 25°C. A white vinyl sticker was placed on the bottom of the plate. 10 μ l/well of 10x NT, SBI-810, or SR142948A treatments were added 10 min prior to reading. 10 μ l/well of 10x coelenterazine 400a (final concentration 7.5 μ M Cayman Chemical Co., Ann Arbor, MI, USA) was added 5 minutes prior to reading. After treatment with coelenterazine 400a, plates were protected from light. For SBI-810 and NT combination studies, cells were incubated in 70 μ l/well HBSS and pre-treated with 10 μ l 10X SBI-810 pretreatments 10 min prior to NT application. Plates were read on a Spark Cyto microplate reader (Tecan Group Ltd., Männedorf, Switzerland) at room temperature in ambient air every 5 min for 20 min. Light was collected between 415–485 nm (Rluc8) and 505–530 nm (GFP2). BRET2 ratios were computed as the ratio of GFP2 to RLuc8 emission. The Δ net BRET ratio was calculated by subtracting the stimulated GFP2/Rluc8 ratios from control GFP2/Rluc8 ratios for each read. The minimum Δ net BRET ratio over time was averaged within treatments and combined between experiments. Data were multiplied by -1 and presented as mean Δ net BRET ratio \pm SEM from at least three independent experiments.

NTSR1 mutagenesis and β -arrestin recruitment assay in HEK293 cells

DNA constructs of wild-type *NTSR1* and mutant *NTSR1* with R166A mutation were synthesized by Twist Bioscience (South San Francisco, CA). Small Bit sequence was linked to pTwist CMV-human NTSR1 WT-SmBit and pTwist CMV-human NTSR1 R166A-SmBit genes. pcDNA3.1-V5-Arrestin2 (Cat. No: 201493), pcDNA3.1-Arrestin2-V5 (Cat. No: 201494), and pcDNA3.1-NabV5-LgBit (Cat. No: 201476) constructs were purchased from Addgene. HEK293 cells were transfected with the three constructs using Lipofectamine 3000 (Invitrogen) and incubated with SBI-810 (0.1 nM–100 μ M) for 1 h. Luminescence was measured using the Infinite 200 Pro Reader (Tecan) after application of 7.5 μ M coelenterazine 400a (Cayman), and the results were normalized to the baseline luminescence of vehicle-treated cells.

Nav1.7 pull down and ubiquitination detection in mouse DRG

SBI-810 (10 μ g i.t.) or vehicle-treated mouse DRG were harvested, washed once in ice-cold PBS, and then scraped in harvest buffer (10 mM HEPES, 100 mM NaCl, 5 mM EDTA, 1 mM benzamide, protease inhibitor tablet, 1% Triton X-100, pH 7.4). Cell lysates were solubilized and immunoprecipitated using an anti-Nav1.7 antibody (Alomone Labs, Rabbit, 1:50, Cat. No: ASC-027) or normal rabbit IgG (Santa Cruz, 1:50, Cat. No: sc-2027). Antibody-binding proteins were pulled down using protein G-conjugated magnetic beads (Promega Cat. No: G7417) and washed through repeated centrifugation and homogenization.

Western blot in mouse DRG and spinal cords

Protein samples were prepared from DRG and spinal cord tissues after SBI-810 or vehicle-treated mice. Tissues were placed on ice and lysed with ice-cold RIPA buffer (Sigma) with protease Inhibitor Cocktail Tablet (pH 7.4) (Roche Diagnostics). The cell lysates and pull-down proteins were centrifuged to remove insoluble debris, and the protein level was detected via BCA assay. The supernatant was mixed with 4x Laemmli buffer (BioRad) and boiled for 30 min (70 °C to reduce Bis-Tris PAGE). Protein samples were electroporated on 4–20% gradient SurePAGE™ Bis-Tris gel (Genscript) and blotted on a PVDF membrane (BioRad). Ponceau S staining was used to detect total proteins. The primary antibody was incubated with 1% BSA at 4°C overnight. We used the following primary antibodies: anti-NR2B antibody (NeuroMab, Mouse, 1:500, Cat No. 75-097), anti-Nav1.7 antibody (Alomone Labs, rabbit, 1:1000, Cat No. ASC-008), anti-Ubiquitin antibody (Santa Cruz, mouse, 1:500, Cat No sc-8017), and anti-GAPDH antibody (Proteintech, Mouse, 1:5000, 60004-1-Ig). Blots were further incubated with an HRP-conjugated secondary anti-rabbit antibody (Santa Cruz, mouse, 1:2000, Cat No. sc-2357) or m-IgG Fc BP-HRP (Santa Cruz, 1:5000, Cat No. sc-525409), and developed in ECL solution (Pierce). The blots were visualized in an Azure 600 image system. Protein signal intensity was quantified by Image J.

Quantitative real-time RT-PCR in mouse spinal cords

Spinal cord tissues were rapidly isolated under RNase-free conditions. Total mRNA was extracted using the RNeasy Plus Mini Kit (74106, QIAGEN) and quantified with a NanoDrop spectrophotometer (Thermo Fisher Scientific). cDNA synthesis was performed using the Reverse Transcription System (3500, Promega). qPCR was conducted on a QuantStudio 3 Real-Time PCR System (Thermo Fisher Scientific) using HotStart™ 2 x Green qPCR Master Mix (K1070, ApexBio Technology). The primer sequences used for qPCR of *Arrb2* were listed in Oligonucleotides. The qPCR results were normalized to *Actin* expression.

Immunohistochemistry (IHC) in mouse DRG and spinal cords

Mice were deeply anaesthetized with isoflurane and transcardially perfused with PBS followed by 4% paraformaldehyde. Lumbar DRG and spinal cord segments (L4–L5) were isolated and post-fixed overnight, and incubated in a sucrose gradient (20–30%). Tissues were then embedded in OCT medium (Tissue-Tek) and cryosectioned with 20 μ m-thick DRG sections and 30 μ m-thick spinal cord free-floating sections. The sections were blocked with 5% goat serum for 1 h at room temperature and then incubated overnight at 4 °C with primary antibodies, including anti-HA antibody (rabbit, 1:300), anti-NeuN antibody (pig, 1:1000), and anti-pERK antibody (rabbit, 1:200, Cell Signaling). The sections were washed in PBS and incubated with the following secondary antibodies conjugated with FITC (anti-pig, anti-rabbit, 1:400) or Alexa 647 (1:400, anti-pig) for 2 h at room temperature. The sections were then washed with PBS and mounted in fluorescent mounting medium and observed under a confocal laser scanning microscope (Zeiss LCM 880 confocal microscope). High-resolution images were obtained from 63x oil magnification.

pERK staining was also conducted in spinal cord slices, which were stimulated with NMDA and then fixed with 4% paraformaldehyde for 1 h. In brief, fresh transverse spinal cord slices (500–600 μm) were cut on a vibratome and perfused with artificial cerebrospinal fluid (ACSF) for 1 h before experiments. Spinal cord slices were incubated with NMDA or/and NMDA receptor antagonists. After treatment, the slices were fixed with 4% paraformaldehyde at room temperature for 1 h then at 4 $^{\circ}\text{C}$ overnight. These slices were then cut on a cryostat (30 μm) for pERK and NeuN IHC, as described above. The number of pERK-positive neurons in the superficial dorsal horn (laminae I–III) were calculated with a computer-assisted imaging analysis system (ImageJ; NIH, Bethesda, MD). Approximately, 6 spinal cord slices were collected from L4–L5 segment per mouse and 6–12 spinal cord sections for each slice were included for pERK quantification.

In situ hybridization (ISH) and double staining with IHC in mouse spinal cords

Tissue samples were prepared the same way as for IHC. Tissues were then embedded in OCT medium (Tissue-Tek) and cryosectioned with 25 μm -thick spinal cord sections. *In situ* hybridization was performed using the RNAscope system (Advanced Cell Diagnostics) following the manufacturer's instructions.⁸⁹ Probes against murine *Ntsr1* (422411-C1) and *Ntsr2* (452311-C2) followed by NeuN immunostaining (Jackson ImmunoResearch, 106-095-003). All images were acquired with the same settings, 4 sections from each animal were selected, and a total of four animals were included for data analysis. QuPath software was used for the quantification. Total neuron numbers were determined by counting DAPI⁺ nuclei in spinal cord sections.

Proximity ligation assay (PLA) in cultured mouse DRG and spinal cord neurons

PLA was performed using Duolink reagents on cultured mouse DRG and spinal cord neurons, as previously reported.⁴⁹ DRG were aseptically extracted from 4-week-old mice and digested for 60 min with collagenase (1.25 mg/ml, Roche) and dispase-II (2.4 units/ml, Roche). The cell suspension was filtered through a 75 μm nylon mesh and then centrifuged at 300 \times g for 5 minutes. The pellet was resuspended and plated onto glass coverslips (Corning 354087). After incubating at 37 $^{\circ}\text{C}$ with 5% CO_2 /95% air for 60 min, the cells were cultured in Neurobasal medium supplemented with 10% FBS, 2% B-27, 1% N-2, and 1% penicillin/streptomycin at 37 $^{\circ}\text{C}$ with 5% CO_2 /95% air for 24 h before conducting experiments. Spinal cord neuron cultures were obtained from WT and NTSR1-HA reporter mice (one-day old, P1). After euthanizing the mice with isoflurane, the spinal column was dissected, and the spinal cord was flushed out with PBS using a syringe. The spinal cords were then minced and digested in 0.25% trypsin at 37 $^{\circ}\text{C}$ for 8 min. An equal volume of DMEM was added to terminate the digestion. The resulting cell suspension was filtered through a 75 μm nylon mesh and centrifuged at 1000 rpm for 3 min. The pellet was resuspended and plated onto glass coverslips. After 5–6 h, the primary cultures were switched to Neurobasal medium. The cultures were maintained at 37 $^{\circ}\text{C}$ with 5% CO_2 /95% air for 24 hours before conducting experiments. DRG and spinal cord neurons were fixed with 4% paraformaldehyde for 15 min at room temperature. PLA was conducted according to the Duolink PLA Protocol from Sigma-Aldrich to examine possible interactions for NTSR1/Nav1.7 and NTSR1/NR2B. Briefly, cells on coverslips were blocked with Duolink Blocking solution for 1 h at 37 $^{\circ}\text{C}$ and incubated with a mixture of two primary antibodies (1:200 mouse anti-HA, rabbit anti-Nav1.7 or 1:200 rabbit anti-HA, mouse anti-NR2B) overnight at 4 $^{\circ}\text{C}$. After incubation, the coverslips were washed with wash buffer A and then incubated with secondary antibodies (anti-mouse MINUS probe and anti-rabbit PLUS probe) for 1 h at 37 $^{\circ}\text{C}$. Coverslips were then washed with wash buffer A and incubated with PLA ligase in ligation buffer for 30 min at 37 $^{\circ}\text{C}$. After incubation, coverslips were washed with wash buffer A and incubated with the polymerase in amplification buffer for 100 min at 37 $^{\circ}\text{C}$, then washed with wash buffer B followed with 0.01 \times wash buffer B for 1 min. Coverslips were mounted in mounting medium containing DAPI (Sigma-Aldrich) and images were captured using a Zeiss LCM 880 confocal microscope. The negative control was conducted with WT control mice.

Flow cytometry analysis in mouse DRG and spinal cord

Mouse DRG and spinal cord tissues were dissociated with 1 mg/ml Collagenase/Dispase (Roche) in a shaking incubator for 90 min. The dissociated tissues were incubated in 10% FBS-supplemented DMEM media for 1 h to neutralize the enzymes. The dissociated cells were washed using a PBS + 10 mM EDTA solution. All dissociated cells were blocked with Fc receptors staining buffer (1% anti-mouse CD16/CD32, 2.4 G2, 2% FBS, 5% NRS, and 2% NMS in HBSS; BD Bioscience) and then stained with a standard panel of antibodies: GLAST-PE (rat-IgG, Cat No.130-118-483, 1:200, Miltenyl Biotech), CD45-FITC (rat IgG, cat No.11-0451-82), Nav1.7-APC (Human IgG, 1 $\mu\text{g}/\text{ml}$), and IgG-APC (Human IgG, Cat No. 403505, 1:200, Biolegend) for mouse DRG or NR2B-APC (mouse IgG, Cat no. 75-097, 1 $\mu\text{g}/\text{ml}$, NeuroMab), GluNA1 -APC (Rabbit IgG, Cat No. 13185, 1:200, Cell signaling), GluNA2-APC (Rabbit IgG, Cat No. 13607, 1:200, Cell signaling), IgG-APC (mouse IgG, Cat No. 130-113-758, 1:200, Miltenyl Biotech) for mouse spinal cord. Nav1.7, NR2B, GluNA1, and GluNA2 antibodies were conjugated with APC using Lightning-Link[®] APC Antibody Labeling Kit (Novus, Cat No.705-0010). After staining, cells were washed in PBS with EDTA. Notably, the surface expression of Nav1.7, GluNA2B, and GluNA1/GluNA2 was identified with antibodies recognizing the extracellular domains of these channels and receptors. The flow cytometry events were acquired in a BD FACS Canto II flow cytometer by using BD FACS Diva 8 software (BD Bioscience). Data were analyzed using Cytobank Software (<https://www.cytobank.org/cytobank>).

Preparation of the mouse spinal cord slices and whole-cell patch-clamp recordings

As we previously reported,⁹⁰ the L4–L5 segment of the lumbar spinal cord was removed from mice under urethane anesthesia (1.5 to 2.0 g/kg, i.p.) and placed into a pre-oxygenated (95% O_2 and 5% CO_2) ice-cold dissection solution (240 mM sucrose, 25 mM

NaHCO₃, 2.5 mM KCl, 1.25 mM NaH₂PO₄, 0.5 mM CaCl₂, and 3.5 mM MgCl₂). Transverse slices (300–400 μm) were prepared using a vibrating microslicer (VT1200S; Leica). The slices were incubated in artificial cerebrospinal fluid (ACSF; 126 mM NaCl, 3 mM KCl, 1.3 mM MgCl₂, 2.5 mM CaCl₂, 26 mM NaHCO₃, 1.25 mM NaH₂PO₄, and 11 mM glucose, equilibrated with 95% O₂ and 5% CO₂) at 32 °C for 30 min prior to experimentation. Subsequently, the spinal cord slices were placed into a recording chamber, were completely submerged, and perfused at a flow rate of 2 to 4 mL/min with pre-oxygenated ACSF at room temperature. Lamina II neurons in lumbar segments were identified as a translucent band under an inverted microscope (BX51WIF; Olympus). We conducted whole cell patch-clamp recordings from the outer lamina II (Ilo) neurons using patch pipettes fabricated from thin-walled and fiber-filled capillaries in voltage-clamp mode. The patch pipette solution for monitoring spontaneous excitatory post-synaptic currents (sEPSCs) contained 135 mM K-gluconate, 5 mM KCl, 0.5 mM CaCl₂, 2 mM MgCl₂, 5 mM EGTA, 5 mM HEPES, and 5 mM Mg-adenosine triphosphate (pH 7.3 adjusted with KOH, 300 mOsm). The resistance of a typical patch pipette was 5–10 MΩ. After establishing the whole-cell configuration, we held neurons at -70 mV to record sEPSCs. Total NMDA currents were recorded in Ilo neurons by perfusing spinal cord slices with 50 μM NMDA for 30 s at the potential of -40 mV. Spinal cord slices had been pre-treated with SBI-810 for 30 min prior to NMDA current recordings. We amplified membrane currents with an Axopatch 700B amplifier (Axon Instruments) in voltage-clamp mode. Signals were filtered at 2 kHz and digitized at 5 kHz. The data were stored with pCLAMP 10.3 software and analyzed with Mini Analysis Program version 6.0.3 (Axon Instruments). All drugs were bath-applied to spinal cord slices by gravity perfusion with a three-way stopcock.

Whole-cell patch clamp recordings in dissociated mouse DRG neurons

Neurons were dissociated, plated, and cultured using the same protocol for Ca²⁺ imaging. Whole-cell voltage-clamp recordings in small-sized DRG neurons (< 25 μm in mice) were conducted at room temperature. Signals were acquired using an Axopatch 700B amplifier. The action potentials were evoked by current injection steps from 0–130 pA with an increment of 10 pA in 600 ms. The data were stored and analyzed with a PC using pCLAMP 10.6 software. Patch pipettes with a pipette solution contained (in mM): 126 potassium gluconate, 10 NaCl, 1 MgCl₂, 10 EGTA, 2 Na-ATP, and 0.1 Mg-GTP, adjusted to pH 7.3 with KOH. The external solution included (in mM): 140 NaCl, 5 KCl, 2 CaCl₂, 1 MgCl₂, 10 HEPES, 10 glucose, adjusted to pH 7.4 with NaOH. In all cases, n refers to the number of the neurons studied from different animals. All drugs were bath-applied by gravity perfusion via a three-way stopcock without any change in the perfusion rate.⁴⁹

Primary culture and whole cell patch clamp recordings from human DRG neurons

Postmortem lumbar human DRG (hDRG) were delivered in ice-cold culture medium within 24–48 h of death. Upon delivery, hDRG were rapidly dissected from nerve roots and minced in a calcium-free HBSS. hDRG were digested at 37 °C in a humidified 5% CO₂ incubator with a collagenase type II (12 mg/ml final concentration; Worthington) and dispase II (20 mg/ml; Roche solution in HBSS for 120 min. hDRG were mechanically dissociated using fire-polished pipettes and centrifuged (500 x g for 5 min). Cells were resuspended, plated on 0.5 mg/ml poly-d-lysine-coated glass coverslips, and grown in culture medium identical to mouse DRG. Twenty-four h after plating, whole-cell patch clamp recordings were performed on small-diameter DRG neurons (<55 μm) at room temperature following the protocol as described for mouse DRG neurons. Action potentials were evoked by current injection steps from 0–130 pA with an increment of 10 pA in 600 ms.

Electromyography (EMG) in mice

Mice were deeply anesthetized with 1.2 g/kg of urethane (i.p.). EMG was used to record C-fiber reflexes from the *biceps femoris*. A pair of needle electrodes was inserted (s.c.) into the medial part of the third and fourth toes. The electrodes delivered electrical stimuli with single-square waves of 1 ms with a constant-current isolated-stimulator to evoke C-fiber reflexes. EMG signals were recorded using a pair of platinum-iridium electrodes inserted into the left *biceps femoris* muscle. A reference electrode was inserted (s.c.) into the tail to decrease signal noise. These signals were amplified by a microelectrode amplifier. The C-fiber reflex threshold (T_c) was identified when the EMG signals corresponding to C-fiber activities were elicited, based on a conduction velocity of 0.4–2 m/s, and the distance between the stimulus and recording sites was calculated. After detecting T_c, the EMG reflex resulting from stimulation at 2 x T_c was established as the nociceptive stimuli. Each C-fiber reflex was recorded over an interval of 5 min.

Computer simulations and *in silico* modeling

The CryoEM structure of human NTSR1 with SBI-553 [PDBID: 8JPB] was used for molecular modeling and dynamics simulations.³⁶ The missing loops in the NTSR1 CryoEM structure were filled with sequences retrieved from the Universal Protein Resource (UniProt) database (ID: P30989).⁹¹ Ligands were drawn and optimized using the molecular building module of the ChemDraw software package. Subsequently, docking of SBI-810 into NTSR1 was performed using AutoDock 4 software.⁹² The UCSF Chimera software (version 1.13.1) was used for the visualization and analysis of the protein structure.⁹³ The binding affinity of each ligand-NTSR1 complex was determined using KDEEP, a protein-ligand binding affinity predictor tool based on 3D convolutional neural networks.⁹⁴ To investigate the stability and dynamic behavior of the protein-ligand complex, molecular dynamics simulations (MDS) were performed using the GPU-accelerated DESMOND software package.⁹⁵ The protein-ligand complex was embedded into a pre-equilibrated 1-palmitoyl-2-oleoyl-sn-glycero-3-phosphocholine (POPC) lipid bilayer to mimic the membrane environment. The membrane-embedded complex was solved in a periodic orthorhombic box filled with explicit TIP3P water molecules. The size of the simulation

box was chosen to ensure a minimum distance of 10 Å between the protein and the box boundaries in all directions. Counterions (Na⁺ or Cl⁻) were added to neutralize the system's net charge. The production MDS was conducted in the NPT ensemble at a physiological temperature of 300K and a pressure of 1.01325 bar (1 atm). To analyze the conformational diversity and identify representative structures from the MDS, the trajectory clustering method implemented in the Desmond software was employed. This method groups similar structures from the simulation based on their atomic root mean square deviation (RMSD). The 1000 trajectory frames from the initial 100 ns simulation were clustered into ten distinct conformational clusters. This clustering enabled the identification of the most frequently occurring and energetically favorable conformations sampled during the simulation. To further assess the stability and robustness of the predicted ligand-protein complex, the three most populous cluster representatives were selected for extended MDS. These simulations were performed using the same protocol as described earlier, but with a significantly longer simulation time of 1000 ns for each of the three selected structures. This extended simulation time permits a more comprehensive exploration of the conformational space and provides insights into the long-term stability of the ligand-protein interactions. The RMSD plots for each of the three extended simulations were generated using the Simulation Interactions Diagram tool in the Desmond software. To provide a consolidated view of the complex stability, the final RMSD plot represented the average RMSD values of all three cluster simulations at each time point over the 1000 ns simulation period. Also see the original simulation data in [Table S3](#).

QUANTIFICATION AND STATISTICAL ANALYSIS

All data are expressed as means ± SEMs. Each data point corresponds to an individual animal in most cases. For electrophysiology data, each data point corresponds to an individual neuron, and neurons were collected from at least three separate animals or donors. We excluded 4 animals from the gabapentin group due to sedative behaviors. Additionally, 3 mice were excluded due to DRG damage after intra-ganglionic injection. In the CPP test, 2 mice were excluded for showing a strong chamber preference during conditioning (spending less than 120 seconds in any chamber, showing an 80% preference). Furthermore, 2 mice were excluded due to mortality following repeated morphine treatment in [Figure 6F](#). All other data were included in the analyses and no outliers were removed. Excluding the mice mentioned above, our study utilized 1306 mice, comprising 696 males and 610 females, alongside 25 rats—13 males and 12 females ([Table S1](#)). Statistical analyses were performed with Prism GraphPad 10. Data were analyzed using two-tailed student's t-test (two groups), one-way ANOVA, two-way ANOVA, or repeated-measures ANOVA (RM-ANOVA),⁷ followed by Bonferroni corrected pair-wise comparisons. The criterion for statistical significance was set at $p < 0.05$.

Supplemental figures

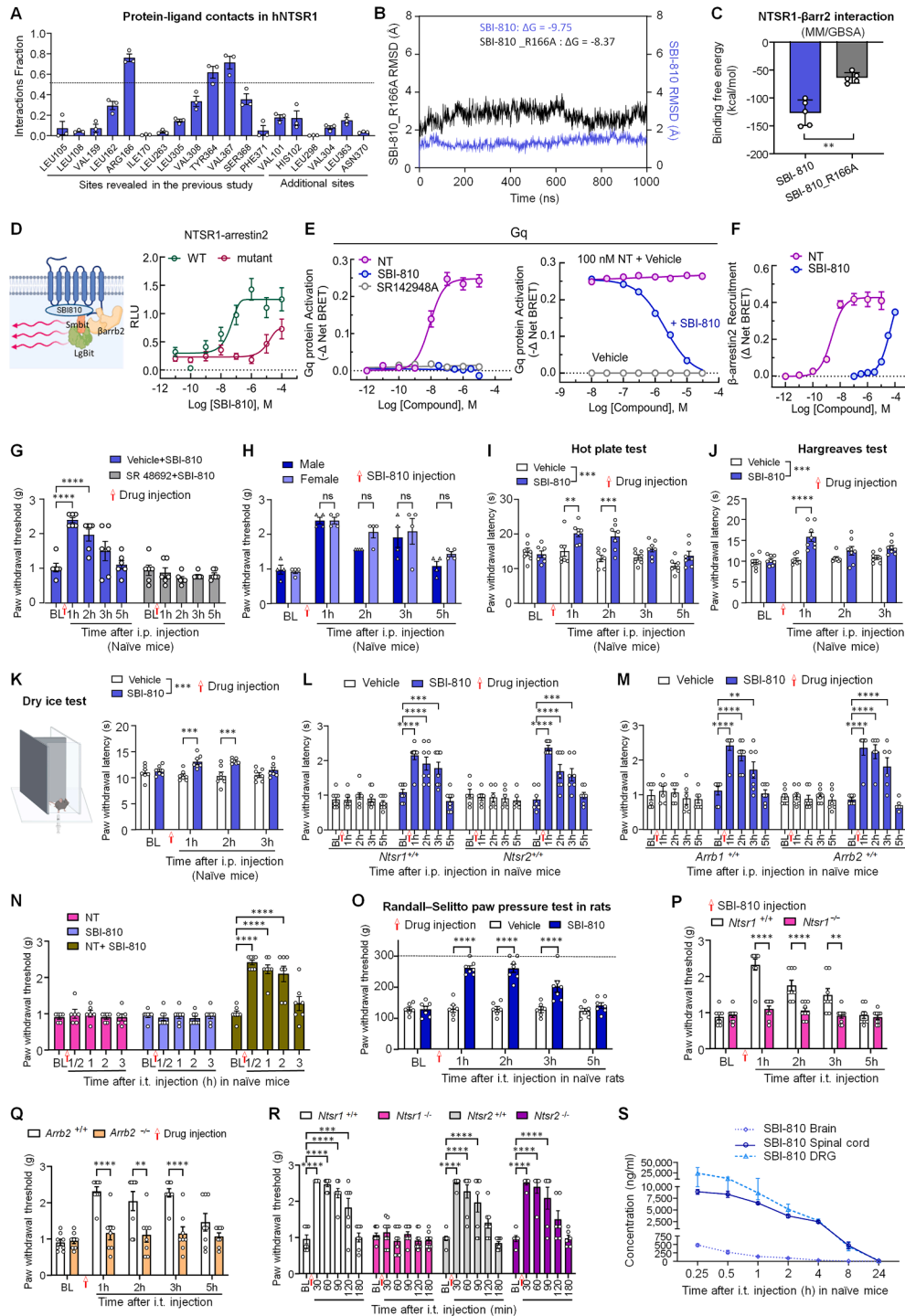


Figure S1. Effects of SBI-810 on acute physiological pain in naive animals, related to Figure 1

(A–C) Computer simulations for SBI-810 interactions with human NTSR1. (A) Interaction fractions showing SBI-810 interaction probability with NTSR1 residues revealed in the previous study³⁶ and additional sites of interactions identified in this study. (B and C) RMSD and ΔG values of SBI-810 (B) following ARG166

(legend continued on next page)

mutagenesis to ALA166. MM/GBSA calculations revealed distinct binding free energy profiles of NTSR1- β arr2 complex between WT and R166A mutant systems (C).

(D) Mutagenesis of NTSR1 from ARG166 to ALA166 reduces SBI-810-evoked β arr2 recruitment. Left, schematic of small bit/large bit binding assay for β arr2. Right, relative light unit (RLU) of β arr2 recruitment in HEK293 cells transfected with WT and mutant *NTSR1*.

(E and F) Effects of SBI-810 on Gq activation and β arr2 recruitment. (E) Gq activation in HEK293T cells expressing human NTSR1. NT stimulates NTSR1-mediated Gq activation, while neither SBI-810 nor SR142948A (negative control) has any effect (left). Note that SBI-810 antagonizes NT-induced Gq activation (right). (F) Comparisons in potency in stimulating β arr2 recruitment to the murine NTSR1. Notably, NT is more potent in stimulating β arr2 recruitment to the receptor than SBI-810.

(G) Blockade of SBI-810-induced increase in PWT by the NTSR1 antagonist SR48692A (1 mg/kg, i.p.). $n = 6$.

(H) Comparison of sex differences in PWT following an injection of SBI-810 (12 mg/kg, i.p.) in male and female mice ($n = 4$).

(I–K) Thermal pain following injection of vehicle and SBI-810 (12 mg/kg, i.p.) in naive mice, as assessed in (I) hot-plate test (I, $n = 7$ for vehicle and SBI-810), Hargreaves test (J, $n = 7$ for vehicle, $n = 8$ for SBI-810), and dry ice test (K, $n = 7$ for vehicle and SBI).

(L) Littermate control mice showing the antinociceptive effects of SBI-810 (12 mg/kg, i.p.) on PWT in *Ntsr1*^{+/+} ($n = 8$ mice/group) and *Ntsr2*^{+/+} mice ($n = 6$ for vehicle and $n = 7$ for SBI-810).

(M) Littermate control mice showing the antinociceptive effects of SBI-810 (12 mg/kg, i.p.) on PWT in *Arrb1*^{+/+} ($n = 6$ for vehicle and $n = 7$ for SBI-810) and *Arrb2*^{+/+} mice ($n = 7$ in vehicle and $n = 6$ in SBI-810).

(N) Effects of i.t. low dose of NT (0.5 μ g, $n = 6$), low dose of SBI-810 (1 μ g, $n = 7$), and their combination (0.5 μ g of NT + 1 μ g of SBI-810, $n = 7$) on PWT.

(O) Randall-Selitto test showing the effects of i.t. vehicle ($n = 6$) and SBI-810 (20 μ g, $n = 7$) on PWT in naive rats.

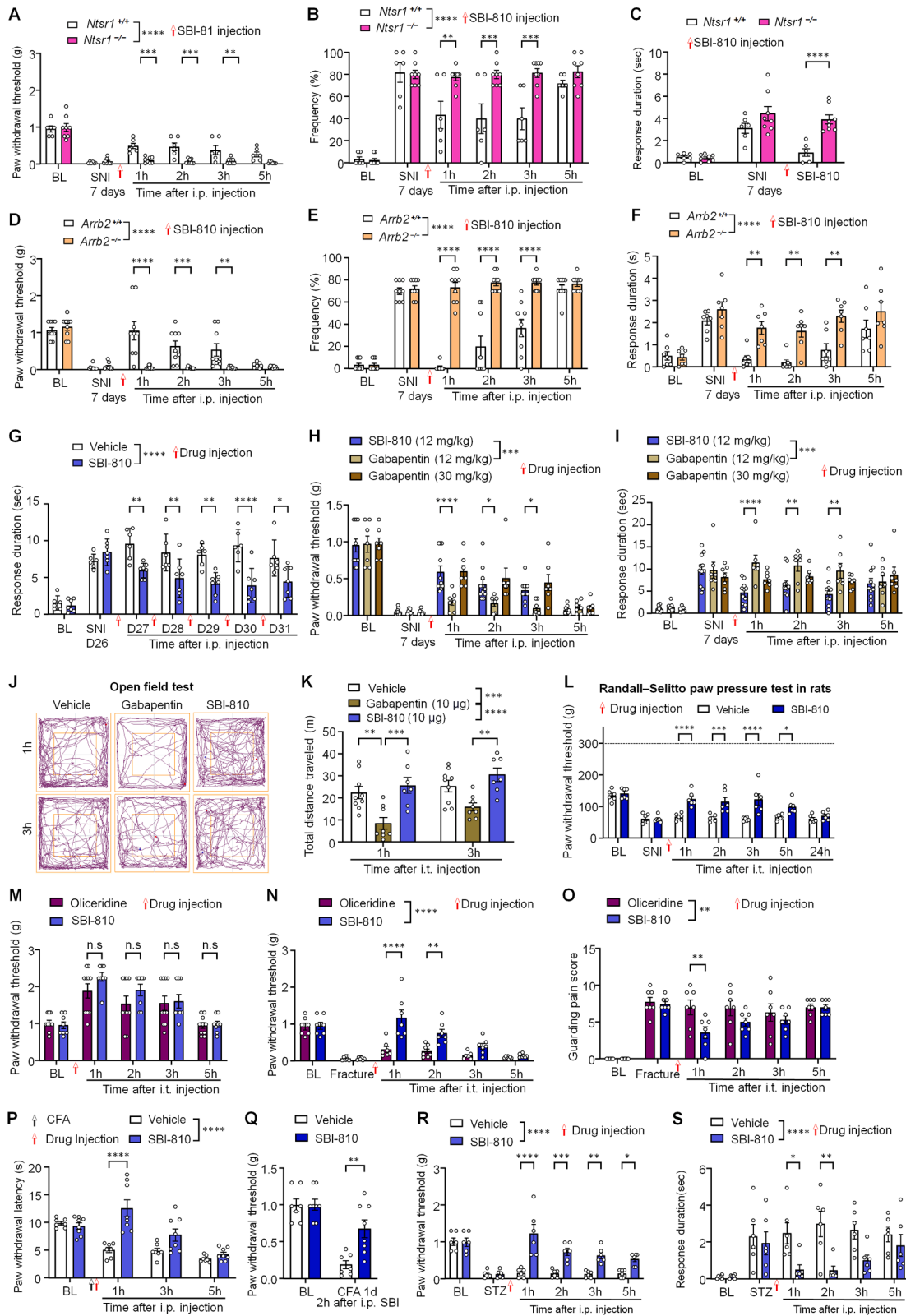
(P and Q) Administration of SBI-810 (10 μ g = 22 nmol, i.t.) increased PWT in *Ntsr1*^{+/+} (P, $n = 8$) and *Arrb2*^{+/+} (Q, $n = 8$) mice but not in *Ntsr1*^{-/-} mice (P, $n = 9$) and *Arrb2*^{-/-} mice (Q, $n = 8$).

(R) NT (22 nmol, i.t.) increases PWT in WT mice (*Ntsr1*^{+/+}, $n = 7$; *Ntsr2*^{+/+}, $n = 8$) and *Ntsr2*^{-/-} mice ($n = 6$) but not in *Ntsr1*^{-/-} mice ($n = 9$).

(S) Pharmacokinetic changes in the concentrations of SBI-810 in the brain, spinal cord, and DRG at 0.25, 0.5, 1, 2, 4, 8, and 24 h following i.t. injection (10 μ g, $n = 4$).

All studies included mice from both sexes, and no sex effects were noted. Red arrows indicate drug injection. Data are presented as means \pm SEMs. * $p < 0.05$, ** $p < 0.01$, *** $p < 0.001$, **** $p < 0.0001$. n.s., not significant. Data were statistically analyzed by unpaired t test (C), two-way RM-ANOVA (G–R), followed by Bonferroni post hoc comparisons.

See also [Table S1](#) for additional details.



(legend on next page)

Figure S2. Effects of systemic or i.t. administration of SBI-810 on neuropathic and postoperative pain in WT and KO mice lacking *Ntsr1* and *Arb2*, related to Figure 2

(A–C) SNI-induced mechanical pain was assessed by PWT (A) and pain withdrawal frequency (PWF, B) and cold pain in acetone test (C) in *Ntsr1*^{+/+} and *Ntsr1*^{-/-} mice after SBI-810 treatment (12 mg/kg, i.p.). *n* = 6 for *Ntsr1*^{+/+} mice and *n* = 8 for *Ntsr1*^{-/-} mice. BL, baseline.

(D–F) SNI-induced mechanical pain of PWT (D) and PWF (E) and cold pain (F) in *Arb2*^{+/+} and *Arb2*^{-/-} mice after SBI-810 treatment (12 mg/kg, i.p.). *n* = 9 mice in (D) and (E) and *n* = 7 mice in (F).

(G) Repeated injections of SBI-810 (12 mg/kg, i.p., *n* = 7; *n* = 6 for vehicle) produced persistent inhibition of cold pain (acetone test) in SNI mice following 5 daily injections. Cold pain was assessed 1 h after each daily injection.

(H and I) Comparisons of the analgesic effects of SBI-810 (12 mg/kg, i.p., *n* = 11) with gabapentin (12 and 30 mg/kg, i.p., *n* = 7) on mechanical pain (H) and cold pain (I).

(J and K) Comparison of the side effects of SBI-810 and gabapentin, as shown in open-field test for the traces of locomotion (J) and the cumulative distance traveled (K) in SNI mice following i.t. treatment with vehicle (*n* = 9), SBI-810 (10 μg, *n* = 8), or gabapentin (10 μg, *n* = 7).

(L) Randall-Selitto test showing SBI-810's antinociceptive effects in SNI-induced mechanical pain in rats (*n* = 6).

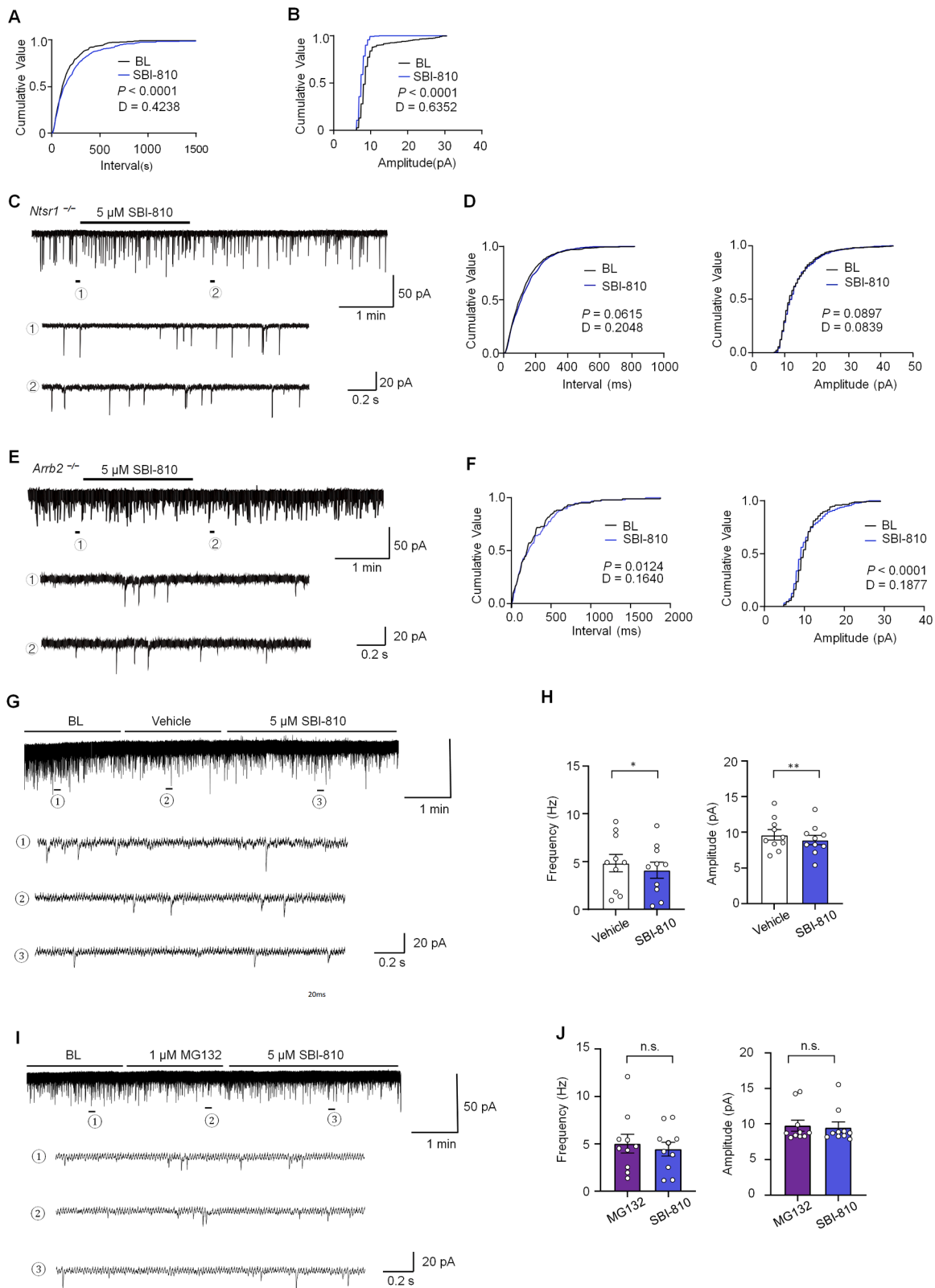
(M–O) Comparison of the analgesic effects of i.t. SBI-810 (10 μg = 22 nmol, *n* = 10) with olliceridine (22 nmol, i.t., *n* = 8) in PWT in naive mice (M) and PWT (N) and guarding behavioral (O) in mice with tibial fracture (*n* = 7).

(P and Q) CFA-induced inflammatory pain was assessed by paw withdrawal latency in Hargreaves test (P) at 1, 3, and 5 h and PWT (Q) at 2 h after vehicle or SBI-810 (12 mg/kg, i.p.) treatment. *n* = 7. BL, baseline.

(R and S) Streptozotocin (STZ) induced neuropathic pain, assessed by PWT in von Frey test (R) and acetone test (S) after systemic administration of vehicle (*n* = 6) or SBI-810 (12 mg/kg, i.p., *n* = 6).

Data are represented as means ± SEMs. Mice from both sexes were tested. Black arrows indicate surgery or CFA injection, and red arrows indicate drug injection. **p* < 0.05, ***p* < 0.01, ****p* < 0.001, *****p* < 0.0001. Data were statistically analyzed by two-way RM-ANOVA (A–I and K–T), followed by Bonferroni-corrected pairwise comparisons.

See also Table S1 for additional details.



(legend on next page)

Figure S3. Effects of SBI-810 on sEPSCs in spinal cord slices from WT, *Ntsr1*^{-/-}, and *Arrb2*^{-/-} mice, related to Figure 3

(A and B) Cumulative values of intervals (A) and amplitudes (B) of sEPSCs in lamina II neurons before (BL) and after SBI-810 treatment, as shown in Figure 3E. sEPSC recordings were conducted in spinal cord slices collected from mice with SNI.

(C and D) Representative sEPSC traces (C) and cumulative values of intervals (D, left) and amplitudes (D, right) of sEPSCs in lamina II neurons before and after SBI-810 treatment in *Ntsr1*^{-/-} mice. sEPSC recordings were conducted in spinal cord slices collected from mice with SNI. The data are quantified in Figure 3F.

(E and F) Representative sEPSC traces (E) and cumulative values of intervals (F, left) and amplitudes (F, right) of sEPSCs in lamina II neurons before and after SBI-810 treatment in *Arrb2*^{-/-} mice. sEPSC recordings were conducted in spinal cord slices collected from mice with SNI surgery. The data are quantified in Figure 3G.

(G–J) Effects of MG132 perfusion on SBI-810's inhibition of sEPSC in SDH neurons of SNI mice. SBI-810 (5 μ M) perfusion significantly reduced sEPSCs frequency (G) and amplitude (H); however, this inhibition on sEPSC frequency (I) and amplitude (J) was prevented by MG-132 pretreatment (1 μ M). $n = 10$ neurons from 4 mice.

Data are shown as means \pm SEMs. Mice from both sexes were included. Data were statistically analyzed by Kolmogorov-Smirnov test (A, B, D, and F) and paired t tests (H and J). * $p < 0.05$, ** $p < 0.01$; n.s., not significant.

See also Table S1 for additional details.

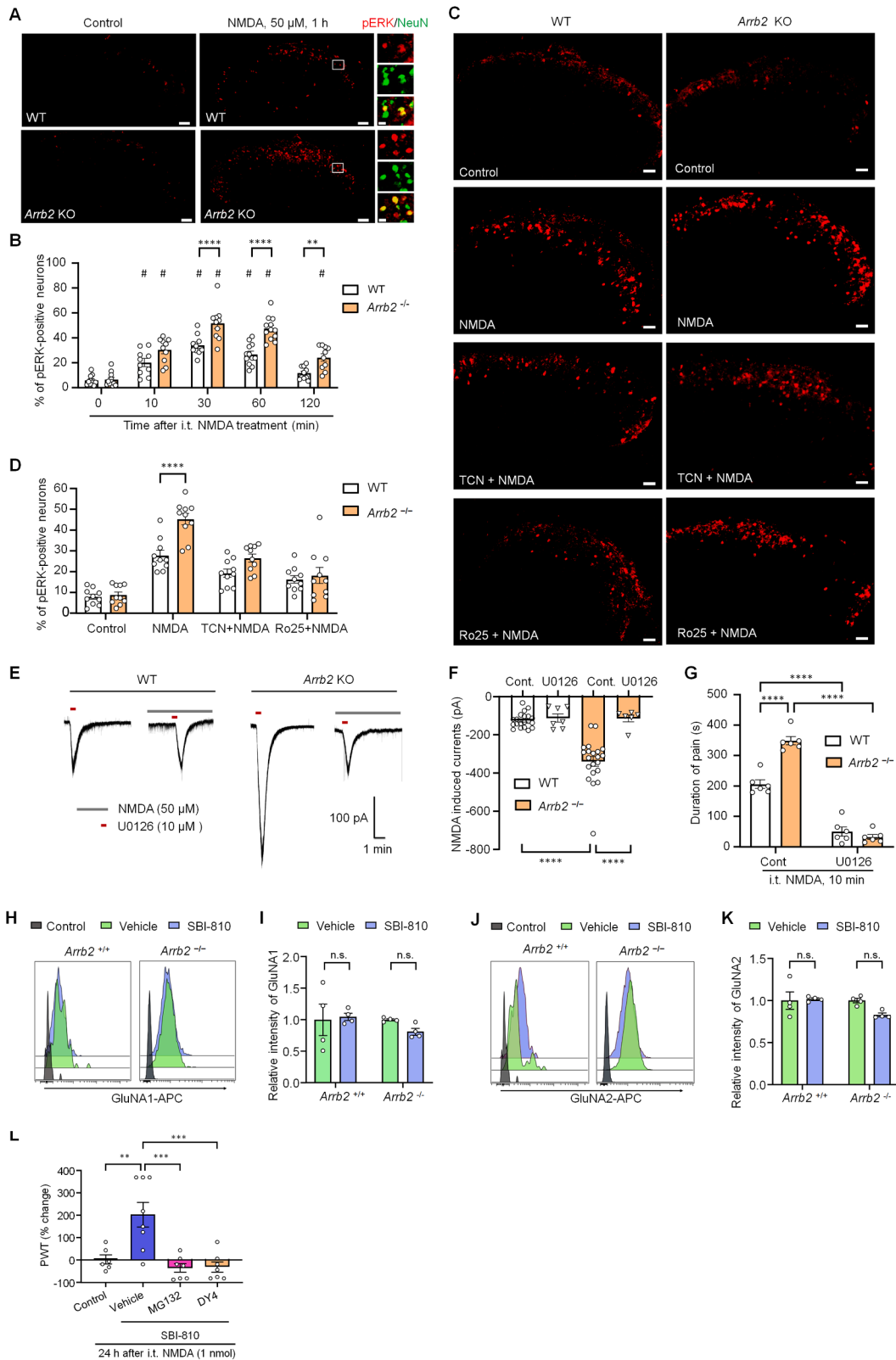


Figure S4. Regulation of NMDAR and ERK activation (pERK) and NMDAR surface expression by β arr2 in SDH neurons of spinal cord slices, related to Figure 4

(A) Photographs of double immunostaining of pERK (red) and NeuN (green) in superficial SDH neurons of WT and *Arrb2*^{-/-} mice after incubation of spinal slices with NMDA alone (50 μ M for 1 h). Scale bar, 50 μ m. Right, enlargement from boxes; scale bar, 10 μ m.

(B) Quantification of the percentage of pERK+ SDH neurons in WT and *Arrb2*^{-/-} mice following NMDA treatment. $n = 10$ –12 slices from 4 mice.

(C) Photographs of pERK immunostaining in SDH of spinal cord slices from WT mice (left) and *Arrb2*^{-/-} mice (right) and the effects of NMDA (50 μ M), the GluN2A antagonist TCN201 (10 μ M), and the GluN2B antagonist Ro 25-6981 (10 μ M). Scale bar, 50 μ m.

(D) Percentage of pERK-positive neurons in superficial SDH of spinal cord slices ($n = 10$ slices from 3 mice). Spinal cord slices were immediately fixed with 4% paraformaldehyde after a 60-min NMDA incubation. $n = 10$ slices from 4 mice.

(E) Representative traces of NMDA (50 μ M)-induced inward currents in lamina II neurons of spinal cord slices from WT and *Arrb2*^{-/-} mice with the ERK blocking effects of U0126 (10 μ M).

(F) Amplitude of NMDA-induced currents of SDH neurons from WT (Cont: $n = 20$; U0126: $n = 7$) and *Arrb2*^{-/-} mice (Cont: $n = 21$; U0126: $n = 6$). $n = 6$ –21 neurons from 3 to 5 mice/genotype/treatment.

(G) NMDA (i.t., 1 nmol) induced spontaneous pain in WT and *Arrb2*^{-/-} mice with the blocking effects of U0126 (i.t., 25 nmol). $n = 6$ mice/group.

(H–K) FACS analysis showing the surface expression of GluNA1 (H and I) and GluNA2 (J and K) in SDH following i.t. SBI-810 (10 μ g) or vehicle treatment in WT mice and *Arrb2*^{-/-} mice. Relative intensities of GluNA1 (I) and the GluNA2 signals (K) were quantified. $n = 4$.

(L) Effects of MG-132 (2.5 nmol, $n = 7$) or DY4 (0.25 nmol, $n = 7$), or vehicle ($n = 8$) on SBI-810's inhibition on mechanical pain induced by NMDA (1 nmol). $n = 6$ for control with NMDA treatment only. The data were presented as % change of PWT.

Data are shown as means \pm SEMs. Data were statistically analyzed by one-way ANOVA (F and L) and two-way ANOVA (B, D, G, I, and K), followed by Bonferroni post hoc corrected pairwise comparisons. ** $p < 0.01$, *** $p < 0.001$, **** $p < 0.0001$. # $p < 0.05$, compared with time 0 BL; n.s., not significant.

See also [Table S1](#) for additional details.

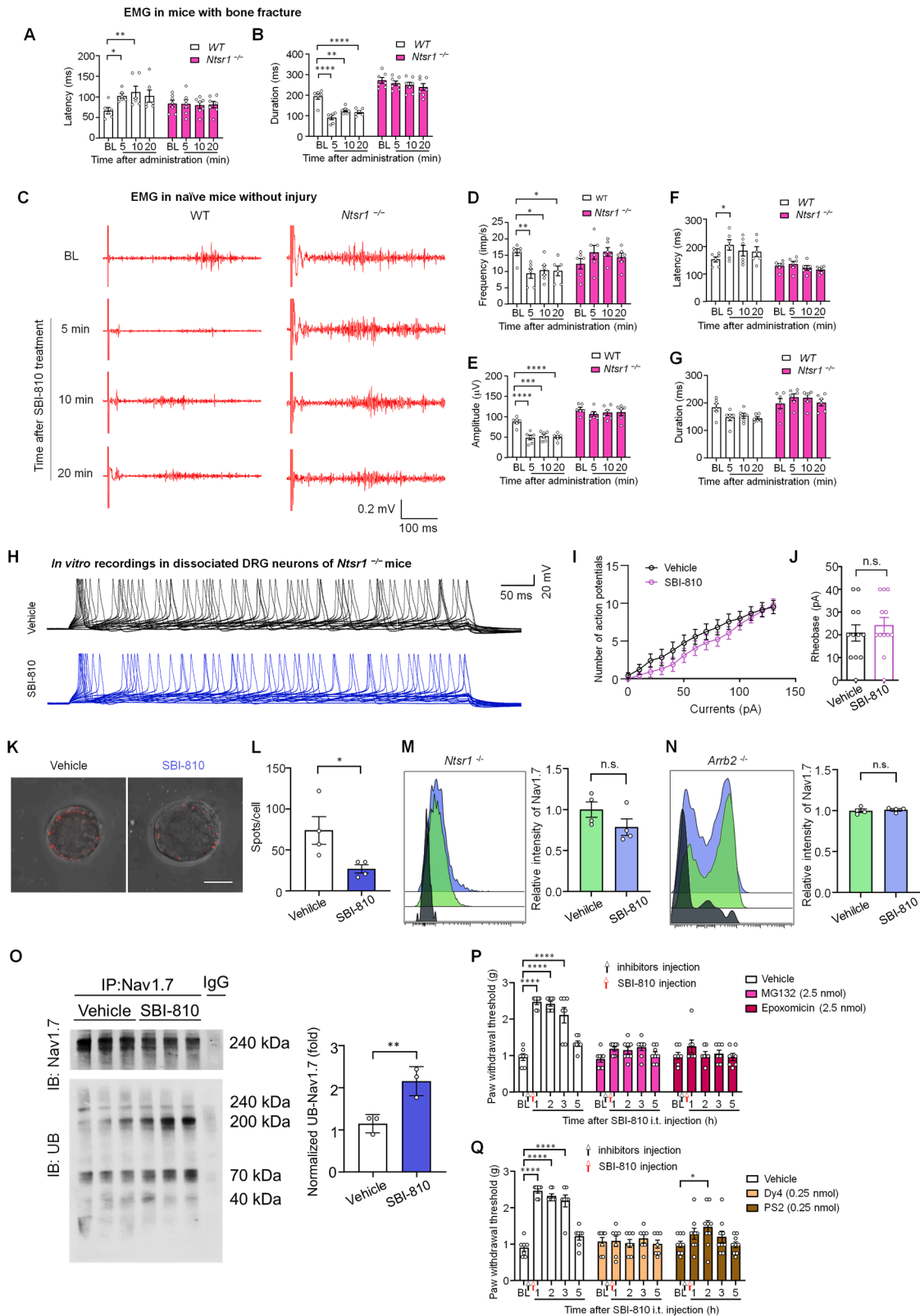


Figure S5. EMG in biceps femoris muscle, AP recordings, and PLA analysis in dissociated DRG neurons, and FACS in DRG, related to Figure 5

(A and B) EMG recordings in *biceps femoris* muscle in WT mice ($n = 6$) and *Ntsr1*^{-/-} mice ($n = 7$) with bone fracture. Quantification shows latency (A) and duration (B) of C-fiber-induced responses in WT and *Ntsr1*^{-/-} mice.

(C–G) EMG recordings in *biceps femoris* muscle in WT and *Ntsr1*^{-/-} mice without bone fracture (naive mice). (C) Representative evoked EMG tracings of C-fiber stimulation at BL and then at 5, 10, and 20 min post-drug treatment in *Ntsr1*^{-/-} mice and WT littermate controls. (D–G) Quantification of frequency (D), amplitude (E), latency (F), and duration (G) of C-fiber-induced responses in WT and *Ntsr1*^{-/-} mice ($n = 6$).

(H–J) Patch-clamp recordings in dissociated mouse DRG neurons with small diameters (<25 μm) from *Ntsr1*^{-/-} mice with SNI. (H) Representative traces of evoked APs and the effects of SBI-810 (5 μM). (I and J) Quantification of the firing rates of APs (I) and rheobase (J) in dissociated mouse DRG neurons ($n = 12$ neurons from 4 mice).

(K and L) PLA showing colocalization of Nav1.7 and NTSR1 (labeled by anti-HA antibody) and the effects of SBI-810 in cultured DRG neurons for 30 min. (K) Representative images, scale bar, 10 μm . (L) Quantification of positive spots per neuron. $n = 4$ cultures.

(M and N) FACS analysis showing the surface expression of Nav1.7 in the DRG of *Ntsr1*^{-/-} mice (M) and *Arrb2*^{-/-} mice (N) following treatment with SBI-810 (10 μg , i.t.), as indicated by the relative expression. $n = 4$.

(O) DRG Nav1.7 pull-down assay showing the effects of SBI-810 (10 μg , i.t.) on Nav1.7 ubiquitination. Immunoglobulin G (IgG) was included as a negative control. Right, quantification of Nav1.7 ubiquitination (intensity of all bands). $n = 3$.

(P) Effects of ubiquitination inhibitor MG132 (2.5 nmol, i.t., $n = 8$) or epoxomicin (2.5 nmol, i.t., $n = 7$), or vehicle ($n = 7$) on SBI-810 (10 μg , i.t.) induced antinociception.

(Q) Effects of endosome inhibitor Dy4 (0.25 nmol, i.t., $n = 7$) or PS2 (0.25 nmol, i.t., $n = 9$) or vehicle ($n = 7$) on SBI-810 (10 μg , i.t.) induced antinociception.

Data are presented as means \pm SEM. Mice from both sexes were included. Data were statistically tested using unpaired t test (J–O) and two-way RM-ANOVA (A, B, D–G, P, and Q), followed by Bonferroni post hoc comparisons. * $p < 0.05$, ** $p < 0.01$, *** $p < 0.001$, **** $p < 0.0001$; n.s., not significant.

See also [Table S1](#) for additional details.

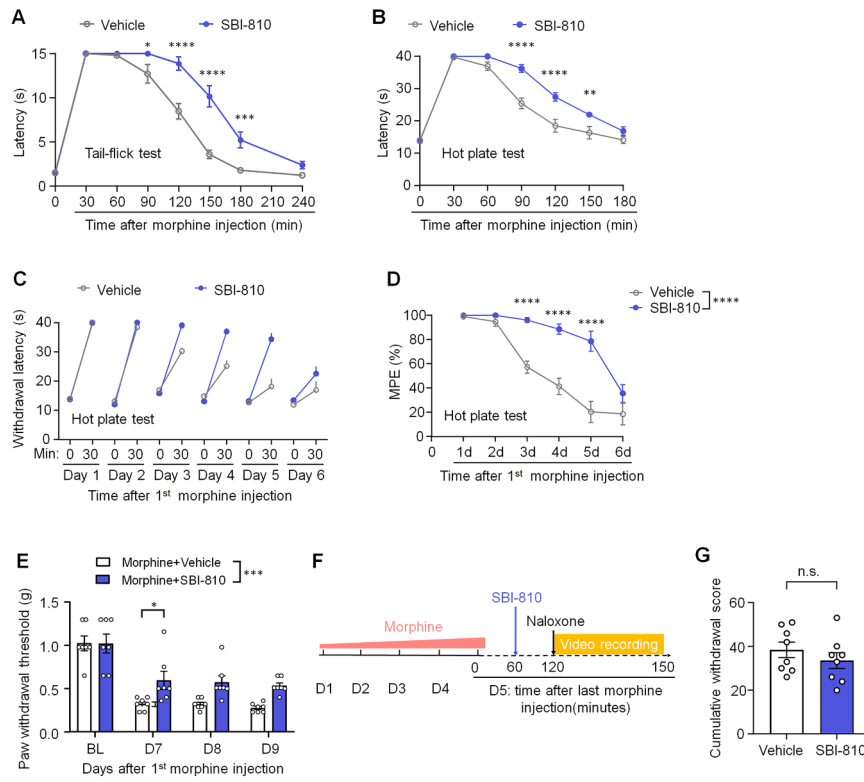


Figure S6. Potentiation of acute opioid-induced analgesia and delay of chronic opioid-induced antinociceptive tolerance by SBI-810, related to Figure 6

(A and B) Tail-flick (A) and hot-plate (B) tests showing acute morphine analgesia (10 mg/kg, s.c.) and comparing the effects of vehicle + morphine ($n = 8$) and SBI-810 (12 mg/kg, i.p.) + morphine ($n = 9$) groups.

(C and D) Hot-plate test showing antinociceptive tolerance induced by chronic morphine treatment (6×10 mg/kg, s.c.; once a day for 6 days), as indicated by withdrawal latency (C) and maximum possible effect (MPE, D). Notably, morphine-induced tolerance is delayed by SBI-810 (6×12 mg/kg, i.p.; once a day for 6 days, $n = 9$), as compared with vehicle treatment ($n = 8$).

(E) von Frey test showing chronic morphine treatment (as in C) induced hyperalgesia, which is mitigated by SBI-810 (6×12 mg/kg, i.p.; twice a day for 6 days, $n = 7$), compared with vehicle ($n = 7$).

(F and G) Effects of post-treatment with SBI-810 (30 mg/kg, i.p.) on chronic opioid-induced withdrawal responses. (F) Schematic of experimental design. SBI was given 60 min after the last morphine injection, followed by naloxone administration (2 mg/kg, i.p.) 60 min later. (G) Cumulative withdrawal score ($n = 8$ mice/treatment). The cumulative score was calculated based on (1) jumping, (2) teeth chattering, (3) wet-dog shakes, (4) head shakes, (5) grooming, (6) paw tremors, (7) piloerection, (8) salivation, and (9) ejaculation.

Data are shown as means \pm SEMs. Mice from both sexes were included. Data were statistically analyzed by unpaired t test (G) and two-way RM-ANOVA (A, B, D, and E), followed by Bonferroni post hoc comparisons. * $p < 0.05$, ** $p < 0.01$, *** $p < 0.001$, **** $p < 0.0001$. n.s., not significant.

See also Table S1 for additional details.